Field Aligned Expansion of Particle Clouds in Magnetically Confined Plasmas: a Lagrangian Model

Paul N. Spathis

IPP 5/38 Januar 1992

MAX-PLANCK-INSTITUT FÜR PLASMAPHYSIK

8046 GARCHING BEI MÜNCHEN

MAX-PLANCK-INSTITUT FÜR PLASMAPHYSIK
GARCHING BEI MÜNCHEN

Field Aligned Expansion of Particle Clouds in Magnetically Confined Plasmas: a Lagrangian Model

Paul N. Spathis

IPP 5/38 Januar 1992

Die nachstehende Arbeit wurde im Rahmen des Vertrages zwischen dem Max-Planck-Institut für Plasmaphysik und der Europäischen Atomgemeinschaft über die Zusammenarbeit auf dem Gebiete der Plasmaphysik durchgeführt.

Field Aligned Expansion of Particle Clouds in Magnetically Confined Plasmas: a Lagrangian Model

Paul N. Spathis

Abstract

A 1-D time-dependent numerical model has been developed for describing the B-parallel expansion of the ablated pellet material in fusion experiments. The hydrodynamic part of the model, which includes, besides the usual conservation equations, also finite rate ionization processes and energy transport by collisional deplation of the flux carried by incident plasma particles, is operational. The computed expansion rates are in agreement with experimental observations.

1. Introduction

A pellet injected into a tokamak traverses a sequence of flux surfaces and, as it continuously erodes, it deposits some fraction of its mass at each flux surface. As a result of the onset of ionization the deposited particles become confined to magnetic flux tubes (whose radii are roughly given by the local values of the ionization radius) and expand along the magnetic field lines, thus distributing the ablated material in both the toroidal and poloidal directions. The time evolution of the density and temperature distributions of the ablated material along the magnetic field lines is of practical interest both for assessing the magnitude and decay time of the disturbance a pellet causes in a tokamak and from the point of view of diagnostics such as $q(r)$ profile measurements by means of pellets.

No information of this kind can be obtained from the steady-state spherically symmetric ablation models presently in use. The objective of this work is to fill this gap. In this report, the hydrodynamic part of the computational model under development and the first results obtained are described.

2. Physical Processes

We now come to briefly review the processes thought to take place when a cryogenic hydrogen pellet is injected into a magnetized fusion plasma. Electrons, moving along the field lines, stream towards the pellet, striking the surface and heating it. Compared with the heat carried by the fast incident electrons, that carried by radiation or incident thermal ions can be shown to be negligible. Heating of the pellet is concentrated in a thin surface layer, driving an evaporation front moving towards the pellet center. Hydrogen molecules leave the pellet surface in a neutral state, establishing a gaseous cloud. Near the pellet surface the flow is believed to be spherical. As the hydrogen molecules stream away from the surface, however, they dissociate and ionize at some point, "sticking" to the field lines. The expansion across the magnetic field therefore stops and further expansion takes place along the field lines. The gas is funneled in a narrow "hose" of a few mm to cm diameter. The energy flux of the incoming electrons is degraded through energy deposition in the ionized and neutral parts of the cloud, thus heating it and accelerating it, while simultaneously the pellet surface is shielded. A quasi-steady state flow results, with the gas expanding in the longitudinal direction against a much lower background pressure. It is this flow, following completion of the transverse expansion, that forms the subject of the present work.

To study the quasi-steady, field-aligned expansion of the cloud, we constructed a one-dimensional, single-fluid, three-species, single-temperature model, incorporating the gas dynamics of the process, energy deposition, and cloud heating by collisional processes and finite ionization rate dynamics.

3. Mathematical Model

The equations defining the model are the mass, momentum, and energy conservation laws governing the cloud hydrodynamic expansion, supplemented by the cloud equation of state and the equations determining ionization and heat conduction.

The heavy-particle continuity equation is

$$\frac{\partial n_h}{\partial t} + \frac{\partial}{\partial z}(n_h v) = \dot{n}_s, \qquad n_h = n_i + n_a, \tag{1}$$

while electron conservation is expressed by

$$\frac{\partial n_e}{\partial t} + \frac{\partial}{\partial z}(n_e v) = \dot{S}_e. \tag{2}$$

Here n_a, $n_i = n_e$ and n_h are the number densities of the neutrals, ions, electrons, and of heavy particles, respectively. The source term $\dot{S}_e$ is the ionization rate and will be specified below, while the mass source strength $\dot{n}_s$ is assumed to be given.

The momentum conservation equation is written in the form

$$\rho\left(\frac{\partial}{\partial t} + v\frac{\partial}{\partial z}\right)v = -\frac{\partial}{\partial z}(p + q_v) + m_s\dot{n}_s(v_s - v) \tag{3}$$

where, ignoring the electron mass

$$\rho = m_n n_h,$$

m_n being the nucleus mass and m_s and v_s the mass and velocity of the source particles. The term q_v represents a pseudo-viscosity contribution to the pressure and is added here to make the numerical scheme used to solve the equations well behaved.

The last equation governing the gas dynamics expansion of the cloud is the energy equation, which takes the form

$$\frac{\partial}{\partial t}\left(\rho\epsilon + \frac{1}{2}\rho v^2\right) + \frac{\partial}{\partial z}\left[\rho\left(h + \frac{1}{2}v^2\right)v\right] = \dot{q}_{int} - \frac{\partial q}{\partial z} + \left(\frac{kT_s}{\gamma - 1} + \frac{1}{2}m_s v_s^2\right)\dot{n}_s. \tag{4}$$

As usual, ϵ and h are the specific internal energy and enthalpy. Coming to the source terms appearing on the right-hand side, q represents the heat flux along the field lines; its structure will be explained in detail later. Transverse heat input shall not be considered for the time being. The energy sink $\dot{q}_{int}$ is the energy spent on ionization and is given by $\dot{q}_{int} = -E_{ion}\dot{S}_e$. For simplicity, the details of the dissociation process are ignored and an effective ionization energy $E_{ion} = 30$ eV will be used in the following. Finally, T_s is the temperature of the source.

By multiplying Eq (3) by v and using Eq (1) an equation for the kinetic energy can be obtained which, on subtraction from Eq (4), gives an equation involving only the cloud thermodynamic properties;

$$\frac{\partial}{\partial t}(\rho\epsilon) + \frac{\partial}{\partial z}(\rho h v) = -E_{ion}\dot{S}_e - \frac{\partial q}{\partial z} + v\frac{\partial}{\partial z}(p + q_v) + \left[\frac{kT_s}{\gamma - 1} + \frac{1}{2}m_s(v_s - v)^2\right]\dot{n}_s. \tag{5}$$

Equation (5) will be used in the following to determine the temperature distribution in the cloud.

The ideal gas law

$$p = (n_a + n_i + n_e)kT = (1+\alpha)n_h kT, \qquad \alpha \equiv n_e/n_h \tag{6}$$

will be taken as the cloud equation of state and, accordingly,

$$\begin{aligned} \epsilon &= \frac{p/\rho}{\gamma - 1} \\ h &= \frac{\gamma p/\rho}{\gamma - 1} \qquad \gamma = 5/3. \end{aligned} \tag{7}$$

The hydrodynamic equations (1)-(3) and (5) and the equation of state (6) are to be solved along with the equations governing internal energy conversion in the cloud, i.e. ionization and heating, to which we now turn.

The ionization rate $\dot{S}_e$ is determined by

$$\dot{S}_e = \alpha_{3b}(T) n_a n_e - \beta_{3b}(T) n_i n_e^2 + \alpha_\nu(T) n_a - \beta_\nu(T) n_i n_e \tag{8}$$

where α_{3b}, α_ν and β_{3b}, β_ν are the coefficients of collisional and radiative ionization and recombination, respectively. At equilibrium the left-hand side of Eq (8) vanishes, while on the other hand, the densities n_a, n_i and n_e must be related by the Saha equation

$$n_i n_e = \left(\frac{2\pi m_e kT}{h^2}\right)^{3/2} \exp(-E_{\text{ion}}/kT) n_a \equiv f_S(T) n_a. \tag{9}$$

The ionization coefficient is therefore related to the coefficient of recombination by

$$\begin{aligned} \alpha_{3b}(T) &= f_S(T)\beta_{3b}(T) \\ \alpha_\nu(T) &= f_S(T)\beta_\nu(T). \end{aligned} \tag{10}$$

Using the above equation and setting $n_i = n_e$, $n_a = n_h - n_e$ in Eq (8), we finally have

$$\dot{S}_e = (\alpha_{3b} n_e + \alpha_\nu)(n_h - n_e - n_e^2/f_S). \tag{11}$$

The approximate expression

$$\alpha_{3b} = \frac{1.64 \cdot 10^{-12}}{E_{\text{ion}} \cdot T^{1/2}} e^{-E_{ion}/T} \text{m}^3 \cdot \text{sec}^{-1} \tag{12}$$

with $E_{\text{ion}} = 30\text{eV}$ (and T expressed in eV) is used to describe collisional ionization [1]. Radiative processes, on the other hand, are described by

$$\beta_\nu = 5.20 \cdot 10^{-20} Z \lambda^{1/2} \left(0.43 + \frac{1}{2}\log\lambda + 0.47\lambda^{-1/3}\right) \text{ m}^3 \cdot \text{sec}^{-1}, \tag{13}$$

where $\lambda = 1.58 \cdot 10^5 Z^2/T(K)$. Equation (13) holds for hydrogen-like ions of nuclear charge Z [2] and will be used in the following with the value $Z = 1.5$, corresponding to a fictitious one-electron atom with ionization energy $E_{\text{ion}} = 30$ eV.

Coming now to the heat flux q affecting the cloud, we represent it as a sum of two parts, a conductive part, q_c corresponding to heat conduction between different regions of the cloud, and a part q_e corresponding to direct energy deposition by the beam of fast, incident electrons:

$$q(z) = q_c(z) + q_e(z).$$

The conductive part is in turn modeled by the sum of the heat flux carried by neutrals, q_a, and that carried by the ionized component, q_i:

$$\begin{aligned} q_a &= -n_a \chi_a k \frac{\partial T}{\partial z}, \qquad \chi_a = 3.8 \cdot 10^{-4} T^{1/2}, \\ q_i &= -n_i \chi_i k \frac{\partial T}{\partial z}, \qquad \chi_i = 4.28 \cdot 10^{-12} T^{5/2}/\log\Lambda, \end{aligned} \tag{14}$$

where χ_a is the neutral conductivity and is the same as that used in [3], χ_i is taken equal to the Spitzer conductivity, and $\log \Lambda$ is the usual Coulomb logarithm. In Eqs (14) T is to be expressed in K and q is given in the usual MKS units of $\text{W} \cdot \text{m}^{-2}$.

We next consider direct energy deposition by the beam of fast, incident electrons. The beam energy is degraded by two mechanisms: electrons lose energy to the cloud by inelastic energy transfer collisions and, in addition, the electron flux is depleted as a result of elastic collisions. To model the effects of the two processes, we proceed by first replacing the incoming beam of a Maxwellian velocity distribution by an equivalent monoenergetic one. It then follows that

$$q_e^\infty = \frac{1}{4} n_e^\infty \bar{v}_e^\infty \cdot E^\infty, \qquad \text{where} \qquad \bar{v}_e^\infty = \sqrt{8kT_e^\infty/\pi m_e}, \quad E^\infty = 2kT_e^\infty. \tag{15}$$

In the above expressions, n_e^∞, T_e^∞ are the background plasma electron number density and temperature, respectively, v_e^∞ and E^∞ are the average background plasma electron velocity and energy, and q_e^∞ is the asymptotic value of the heat flux. Let now $\Gamma_e(z)$, $E(z)$ be the electron flux and average energy as functions of the distance z from the mass source. With these definitions, one obviously has

$$q_e(z) = \Gamma_e(z) E(z), \qquad \frac{1}{q_e}\frac{\partial q_e}{\partial z} = \frac{1}{\Gamma_e}\frac{\partial \Gamma_e}{\partial z} + \frac{1}{E}\frac{\partial E}{\partial z}. \tag{16}$$

In the following we will use

$$\frac{1}{\Gamma_e}\frac{\partial \Gamma_e}{\partial z} = \frac{1}{\lambda^M}, \qquad \frac{1}{E}\frac{\partial E}{\partial z} = \frac{1}{\lambda^E}, \tag{18}$$

where

$$\begin{aligned} \frac{1}{\lambda^M} &= \frac{1}{\lambda_a^M} + \frac{1}{\lambda_i^M} + \frac{1}{\lambda_e^M}, \\ \frac{1}{\lambda^E} &= \frac{1}{\lambda_a^E} + \frac{1}{\lambda_i^E} + \frac{1}{\lambda_e^E}, \end{aligned} \tag{18}$$

and the characteristic lengths for momentum and energy loss of electrons scattered by neutrals, ions, and electrons, λ^M and λ^E respectively, are taken from [4, 5, 6, 7]. Equations (16)-(18), along with the obvious boundary conditions

$$q_e(z) \to q_e^\infty, \quad E(z) \to E^\infty \quad \text{as} \quad z \to \infty$$

completely define the heat flux carried by the incident plasma electrons. Since the energy transfer from the background plasma to the cloud is determined by the stopping length calculations, adiabatic boundary conditions are applied to the heat conduction part.

4. Numerical Method

Equations (1)-(18) were solved numerically. The computer code is a modified version of the one developed for simulating cloud expansion in the transverse (B-perp.) direction [8]. The basic scenario to be modelled is as follows. A source of cold particles ($T_s = 100$ K) of given strength $\dot{n}_s$ (s^{-1}) is located at the inlet section ($z = 0$) of a straight channel (aligned with the magnetic field) of given cross-section. The channel representing a magnetic flux tube is of given length and is filled with a plasma of given state parameters: T_e^∞ and n_e^∞. In the present series of calculations, the channel length is assumed to approach infinity and thus the plasma represents an energy reservoir of constant state parameters. A Lagrangian scheme is used, i.e. the cloud of cold particles is represented by a number of Lagrangian mass cells which expand into the background plasma. The initial cloud size is chosen small enough ($< 1\%$) in relation to the final cloud size. To model mass addition, the mass of the leftmost (i.e. $z = 0$) cell is increased at a constant rate, equal to $m_s\dot{n}_s$. When its mass exceeds the mass of other cells in the system by more than 10%, the cell is "split", i.e. replaced by two new ones, the left of which carries the excess mass in such a way as to conserve total energy and momentum, and the computation resumes. In a similar fashion, in order to keep the required computing time within reasonable limits, whenever the thermodynamic properties of the rightmost two cells approach each other and those of the background plasma within 10%, they are "merged", i.e. replaced by a single new cell in such a way as to conserve mass, momentum and energy.

As a result of the Lagrangian representation used, Eq (1) is automatically satisfied in the part of the system away from the mass source. A second-order-accurate, time-centered Richtmeyer-Von Neumann scheme was used at every time step to advance the

value of the flow velocity v according to Eq (3). The fluid coordinate z can then easily be computed as a function of mass and, from it, the updated value of the density ρ. Expressing ϵ, h in terms of the temperature and substituting in Eq (5) gives an equation for T, to be solved along with the rate equation (11). Since Eqs (5) and (8) are coupled, an implicit, predictor-corrector scheme was used to solve them.

For testing of the hydrodynamic part of the code, ionization, heat conduction and mass addition were "turned off" and the motion of the fluid was blocked at the two ends of the computational domain, thus simulating a shock tube. The initial conditions chosen were $n_h = 10^{25}$ m^{-3}, $p = 8.0 \cdot 10^5$ N $\cdot$ m^{-2} in the left half and $n_h = 10^{25}$ m^{-3}, $p = 8.0 \cdot 10^4$ N $\cdot$ m^{-2} in the right, giving rise to a moderately strong shock on breakdown. The initial temperature was equal to 0.5 eV in both halves of the tube. The computed solution, for which 200 cells were used, is shown along with the analytical one on Fig. 1. The computed shock speed is in error by approximately 2.5%. On the other hand, in the smooth parts of the flow field the two solutions agree to better than one per cent. Naturally, aside from the oscillations behind the shock front, characteristic of linear schemes of order higher than first, oscillations also appear behind the tail of the expansion wave. It should be noted that in the scenario calculations presented in the following section, fewer than 200 cells were used to keep the required computing time within manageable limits. On the other hand, since we expect a rather smooth flow field during the quasi-steady state phase of the cloud expansion, the accuracy of the scheme should be sufficient for our needs.

The heat conduction part of the code was similarly tested by blocking fluid motion, assuming constant number density and "switching off" ionization. The number density was taken to be $n_a = 10^{24}$m^{-3} and the thermal conductivity was assumed to be given by $\chi(T)/n_a k = 1.16 \cdot 10^{-10} T^{5/2}(K)m^2 \cdot$ sec^{-1}, i.e. a pure power law. The total length of the medium was assumed to be 5 mm and was divided into 150 cells. At time $t = 0$ the temperature was assumed to be negligibly small throughout the medium except in the first two cells, where it was taken to be $T = 10$ keV, thus approximating a delta function profile. For these initial conditions and the assumed temperature dependence of χ, an analytic, self-similar solution exists [9]. The computed temperature distribution, along with that given by the analytic solution, is given in Fig. 2 for three different time instants. The agreement is everywhere better than 1% and the small discrepancies are well within the limits implied by the fineness of the grid.

In another series of test calculations, thermal choking of steady-state constant-area channel flows was simulated. As is known, unlike in spherically symmetric ideal flows, where acceleration to supersonic velocities by heat addition is possible [4, 6] the flow in a constant-area channel can be acccelerated by heat addition only up to the sonic velocity. Any further increase of the heat addition rate makes the flow choked, and the the exit flow Mach number remains at unity.
For the purpose of these simulations, the following channel and flow parameters were chosen: channel length L = 1 m, channel radius R = 6 mm, constant particle influx (with negligible internal energy) at the l.h.s. boundary $\dot{N} = 3 \times 10^{22}\ s^{-1}$. A given (conductive) heat flux q_0 was prescribed at the r.h.s. boundary. A variable-mass Lagrangian system was used: new cells were continuously created at the l.h.s. boundary and continuous mass removal took place at the r.h.s. boundary (for method see next

section). Since the masses of the first and last cells were continuously changing in time, the condition of steady state was locally violated there. As a result of this, some small-amplitude oscillations were introduced into the system at the inlet section and, because of the continuously decreasing mass of the last cell, acceleration to supersonic velocities of the last cell interfaces became possible even under choked flow conditions. The location of the last cell interface at which the condition of steady state is still rigorously fulfilled is marked by broken lines in Figs. 3 and 4.

Three scenarios with three different values of q_0 were considered: (a) 0.84×10^{11}, (b) 1.32×10^{11}, and (c) 2.09×10^{11} Wm^{-2}. A set of initial parameter distributions was assumed for the channel, and the computation was continued until the influence of the assumed distributions vanished and quasi-steady parameter distributions were established. Figure 3 shows the Mach number and pressure distributions for case (a). In this case, the heat supply rate is not sufficient for accelerating the flow to sonic velocity. In the case (b), not shown in the figures, sonic velocity was obtained at the location of the last cell boundary fulfilling the condition of constant mass. The distributions shown in Fig. 4 correspond to case (c): although the heat flux is further increased, the Mach number of the last cell interface which still fulfills the steady-state condition remains approximately unity.

5. Numerical Results

In all of the simulations to be presented, flow was assumed to take place in a cylindrical channel of radius 6 mm. The value $n_h^\infty = n_e^\infty = 10^{20} m^{-3}$ was taken for the background plasma electron and ion number densities. The initial cloud density and temperature were assumed uniform throughout the cloud. The initial temperature was always taken to be 0.25 eV, while the initial density was chosen such that the starting cloud mass did not exceed 1% of the total deposited mass. The source was assumed active for 10 μsec, typical of the pellet residence time in a flux tube defined by the ionization radius of the ablated material.

In Figs. 3 and 4 we present the results of our simulations for a source strength $\dot{n}_s = 10^{24}\mathrm{sec}^{-1}$ and a background plasma temperature $T_e^\infty = 1$ keV at times $t = 10$ and 52 μsec, respectively. Profiles are shown of the flow velocity v, local Mach number M, heavy particle and electron number densities n_h and n_e, convective cloud electron number flux $n_e v$, beam electron number flux Γ_e, heat flux carried by the beam, q_e, and conductive heat flux q_c. Similar results are given in Figs. 5 and 6 for $\dot{n}_s = 10^{24}\mathrm{sec}^{-1}$ and $T_e^\infty = 5$keV and times $t = 7.8$ and 52 μsec, respectively, and in Figs. 7 and 8 for $\dot{n}_s = 10^{25}\mathrm{sec}^{-1}$, $T_e^\infty = 5$keV and times $t = 7.7$ and 32 μsec.

A quick look at Figs. 3 through 8 reveals flow velocities up to a few times 10^5m/s at the hot end of the cloud, while in all cases presented the corresponding Mach number is in the range $M = 2$ to 3. Considering Fig. 3, it can be seen that at $t = 10\mu$sec the ionization length is a few centimeters. The temperature near the core is close to the source temperature ($T_s = 100$ K), while it has yet to reach background temperature at the hot end. The above picture can be better understood with the help of the accompanying heat and number density fluxes. It is clear that, for the energy flux available, the mass source strength is high enough to stop the beam electrons before reaching the core. Heat is transported to the core solely by conduction. As a result of the small thermal conductivity of the neutral gas, the conductive heat flux is several

orders of magnitude below the beam electron flux before it is depleted. Thus, a dense cold core forms. The picture is qualitatively the same at $t = 52\mu$sec (see Fig. 4), with two changes: (a) the energy flux is completely depleted 2 m away from the source region (compared with approximately 8 cm at $t = 10\mu$ s), and (b) the temperature of the cloud at the right-hand side boundary approaches the background plasma temperature. The temperature drop at the core is due first to the reduced heat flux and second to the gas dynamic expansion. The beam depletion zone is convected away from the core. As a final remark, we note that the region in which the incident electron flux is depleted does not coincide with the domain in which the cloud electrons are "created", thus calling for electrostatic field considerations (the condition $j = 0$ is to be fulfilled at any z coordinate).

Figures 5 and 6 show the effect of increasing the background plasma temperature (5 keV as compared with 1 keV of Figs. 3 and 4) on the cloud characteristics: as before, the source strength is $10^{24}(\text{sec}^{-1})$. An inspection of the results shown in Fig. 5 at time $t = 7.8\,\mu$sec, corresponding roughly to those of Fig. 3, reveals much higher velocities and temperatures near the core and correspondingly lower densities. As can be seen from the attached Γ_e, q_e, and q_c plots, owing to their higher energy, the beam electrons are not stopped by the cloud, thus depositing their energy throughout it and heating it in a more uniform manner. A significant fraction of the energy flux is not absorbed (shine-through). The picture is qualitatively similar at 52 μsec, long after the mass source has ceased to be active. Once again, conditions at the hot end of the cloud approach those prevailing at the background, while all of the mass deposited is ionized.

As was to be expected, it is obvious from the results shown in Figs. 7 and 8, which correspond to a source strength of 10^{25}sec^{-1} and a background temperature of 5 keV, that increasing mass source strength has an effect to some extent similar to that of reducing the background temperature. At 7.7 μsec the cloud is not massive enough to stop the incident electron beam. Compared with the corresponding results for the lower source strength (10^{24}), the flow velocity and cloud density at the core are an order of magnitude lower and higher, respectively, a fact that we attribute to the higher mass addition rate. Overall, the picture resembles that of the previous case at the same time. Nonetheless, by the end of the 10 μsec during which the source remains active, enough mass has been deposited to shield it from the background plasma. As a result, a dense, cold core forms once again that, even at times as late as 32 μsec, does not "feel" the incoming heat. On the other hand, conditions at the hot end of the cloud are slowly approaching the background ones, albeit at a much slower rate.

A common feature of all these distributions is that the balance between the cold particle source given at $z = 0$ and the energy reservoir (energy flux) conditions specified at the hot end uniquely define the evolution of the $n(z)$ and $T(z)$ distributions. Note that no boundary conditions are specified for n and T at $z = 0$, these function values being "floating", i.e. defined, at any time instant, by the local balance of the mass and energy supply rates. The mass present in the system is steadily increasing: the heat source represented by the undisturbed plasma at the right-hand end of the cloud is shifted further and further from the cold-particle source. The transverse energy flux was assumed to be zero in these calculations.

Before concluding, we note here that in our simulations, the mass source strength $\dot{n}_s$ and the background plasma temperature T_e^∞ are treated as independent input parameters. In reality, the pellet ablation rate (mass source strength) is a function of the energy flux available; the ablation process is self-regulating. Therefore, our computational results are not yet directly applicable to real ablation scenarios.

6. Summary

A 1-D time-dependent numerical model has been developed for describing the B-parallel expansion of the ablated pellet material in fusion experiments. Already operational is the hydrodynamic part of the model, which includes, besides the usual conservation equations, also finite rate ionization processes and energy transport by collisional depletion of the flux carried by incident plasma particles. The computed expansion rates are in agreement with experimental observations (see, for example, Mansfield et al. [10]).

To make the model self-consistent (the next step), will be to include electrostatic field effects in the energy flux depletion calculations. Furthermore, the single-energy pencil-beam approximation used in the stopping length calculations shall be replaced by an approximation involving a discrete number of energy groups corresponding to, for example, a Maxwellian energy distribution in the background plasma.

7. Acknowledgments

It is a pleasure to thank Dr. L. Lengyel on whose ideas the work reported here is based. Thanks are also due to Prof. K. Lackner and Dr. P. Lalousis for many valuable discussions and suggestions.

References

[1] Kolb and McWhirter, Physics of Fluids, **7**, 519 (1964).

[2] Seaton, M. J., Mon. Not. R. Astron. Soc., **119**, 81 (1959).

[3] M. Kaufmann, K. Lackner, L. L. Lengyel and W. Schneider, Nucl. Fusion, **26**, 171 (1986).

[4] P.B. Parks, Nucl. Fusion **20**, 311 (1980).

[5] W.T. Miles, R. Thompson, and A.E.S. Green, J. Appl. Phys. **43**, 678 (1972)

[6] P.B. Parks and R.J. Turnbull, Phys. Fluids **21**, 1735 (1978)

[7] L.L. Lengyel, IPP Report # 1/233, Sep 1984

[8] L.L. Lengyel, IPP Rept. # 5/41, Aug. 1991; see also Phys. Fluids **31**, 1577 (1988).

[9] Zel'dovitch, Ya. B. and Raizer, Yu. P., Physics of Shock Waves and High-Temperature Hydrodynamic Phenomena, Academic Press (1966).

[10] D.K. Mansfield et al, Phys. Rev. Lett., **66**, 3140 (1991).

$t = 4.0\,\mu\text{s}, \quad T = 0.5\,\text{eV}$

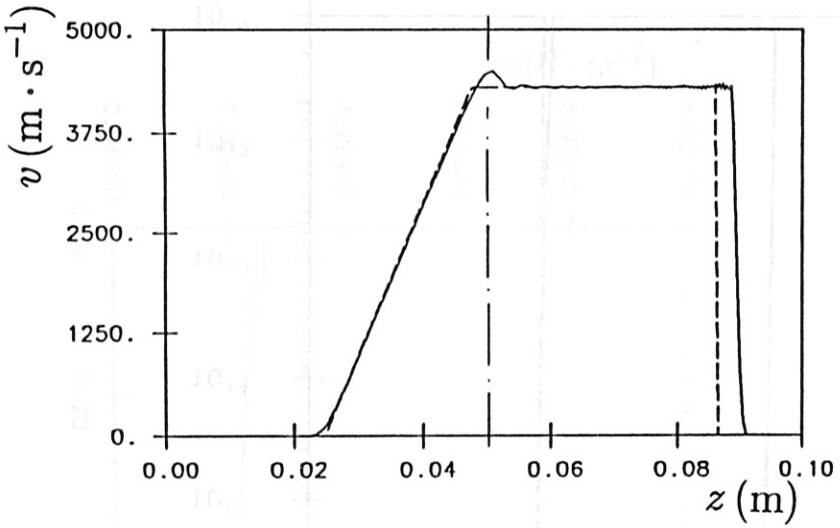

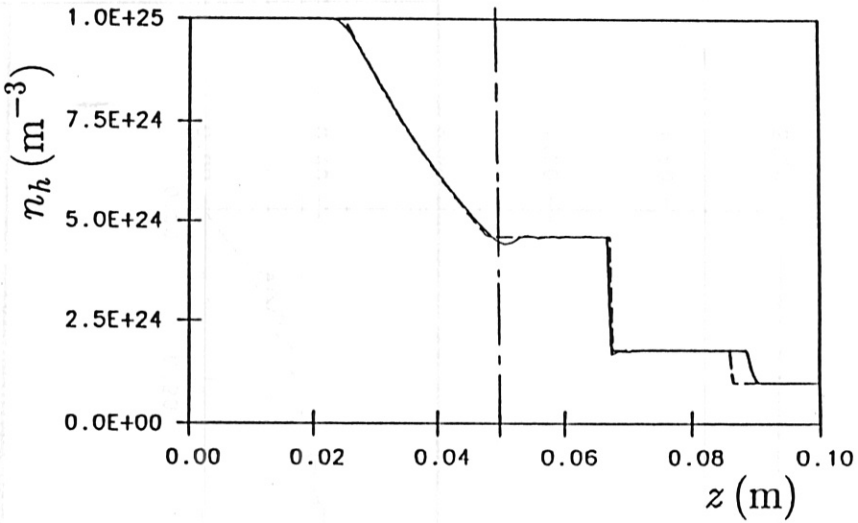

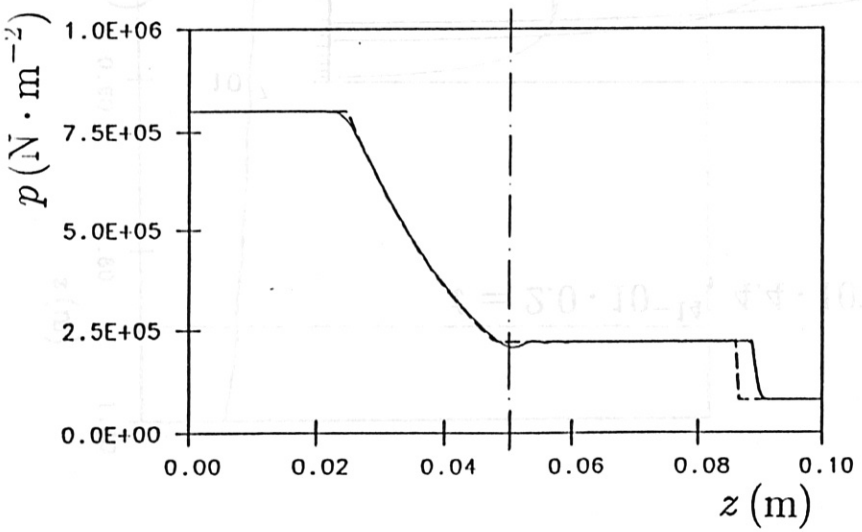

Fig 1

$t = 2.0 \cdot 10^{-14}$, $4.4 \cdot 10^{-13}$ and $2.0 \cdot 10^{-12}$ sec

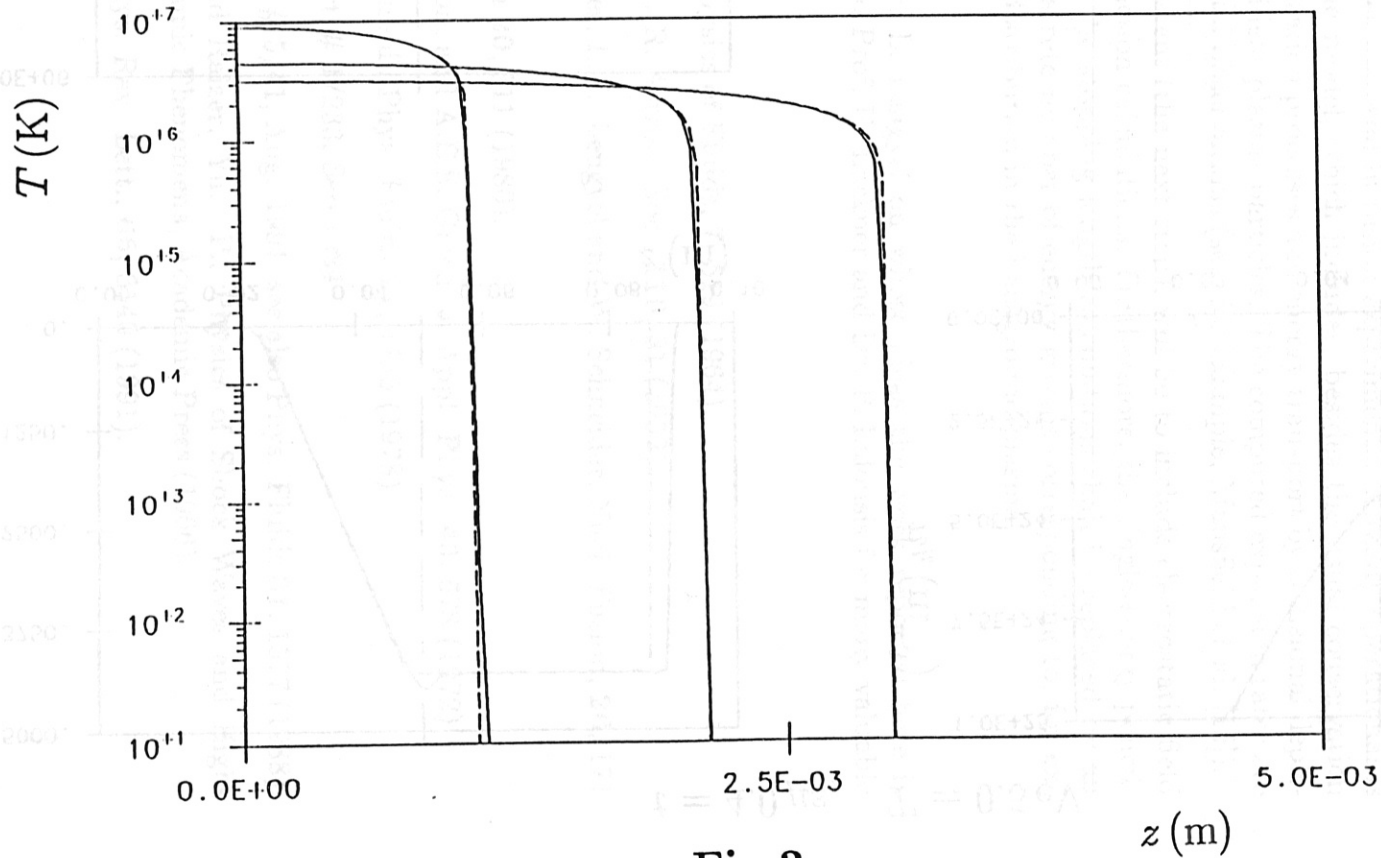

Fig 2

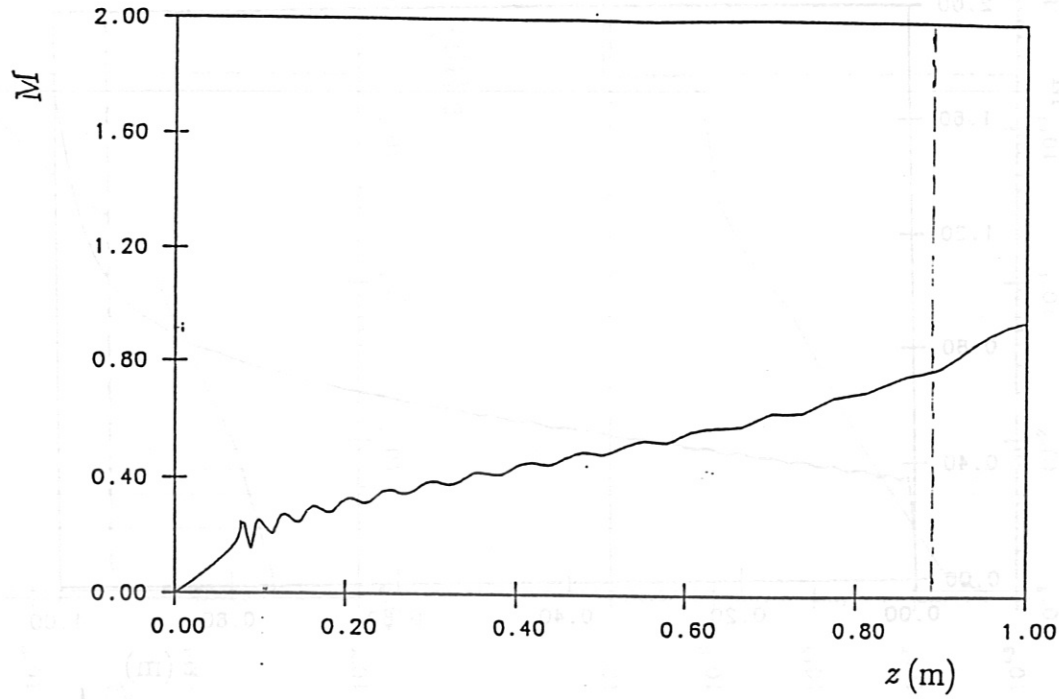
M
2.00
1.60
1.20
0.80
0.40
0.00
0.00
0.20
0.40
0.60
0.80
1.00
z (m)

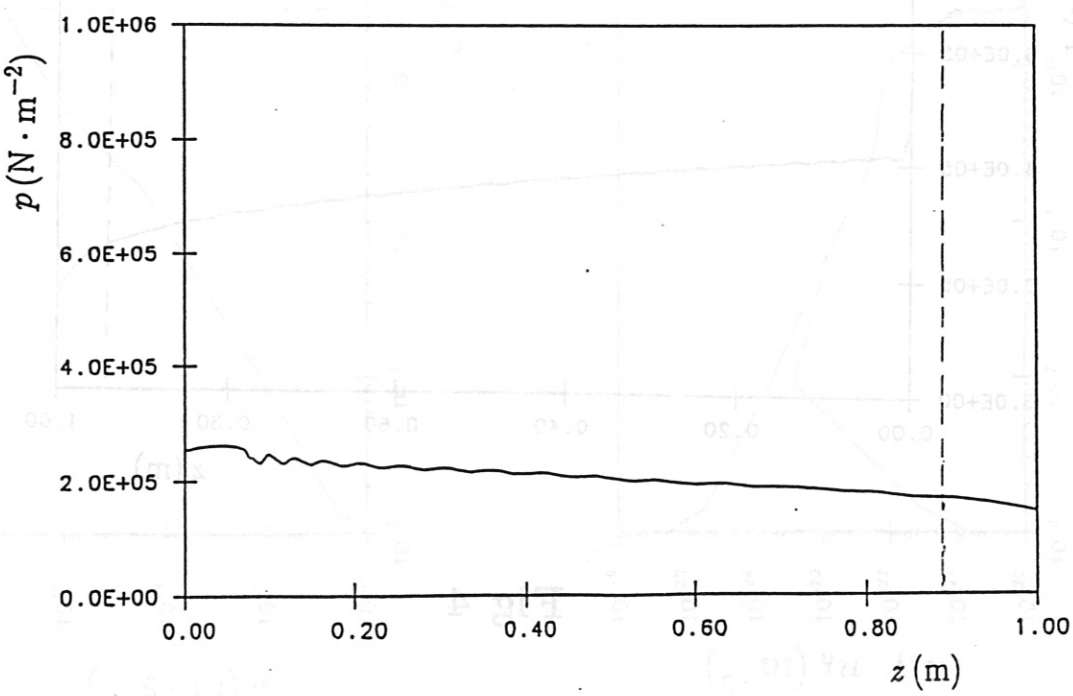
p (N · m⁻²)
1.0E+06
8.0E+05
6.0E+05
4.0E+05
2.0E+05
0.0E+00
0.00
0.20
0.40
0.60
0.80
1.00
z (m)

Fig 3

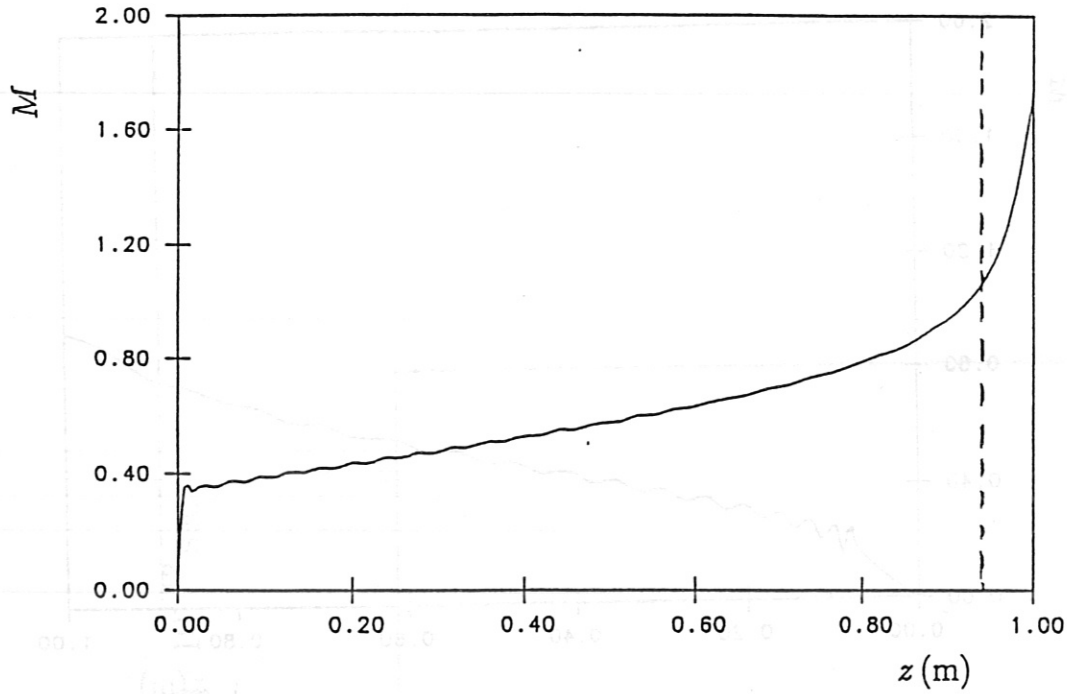
M
2.00
1.60
1.20
0.80
0.40
0.00
0.00
0.20
0.40
0.60
0.80
1.00
z (m)

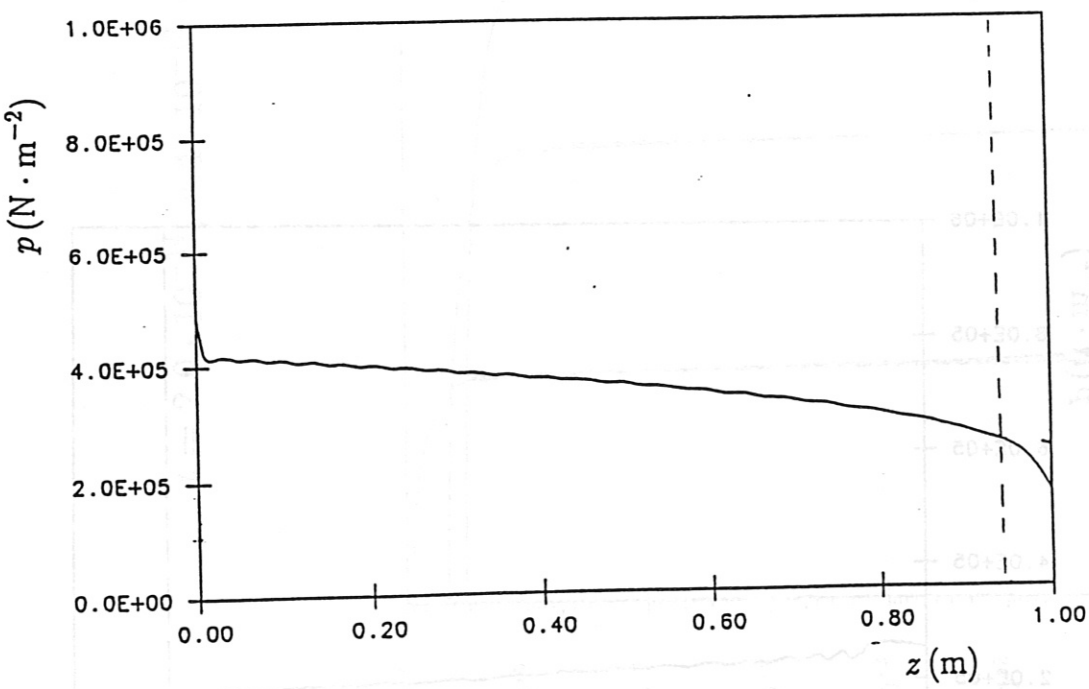
p (N · m⁻²)
1.0E+06
8.0E+05
6.0E+05
4.0E+05
2.0E+05
0.0E+00
0.00
0.20
0.40
0.60
0.80
1.00
z (m)

Fig 4

$$\dot{n}_s = 10^{24}\,\mathrm{s}^{-1}, \quad T_e^{\infty} = 1\,\mathrm{keV}, \quad t = 10\,\mu\mathrm{s}$$

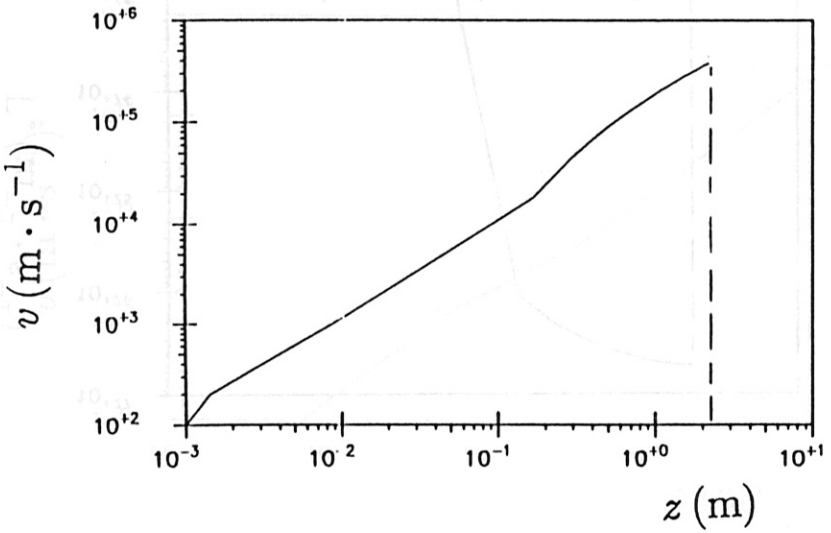

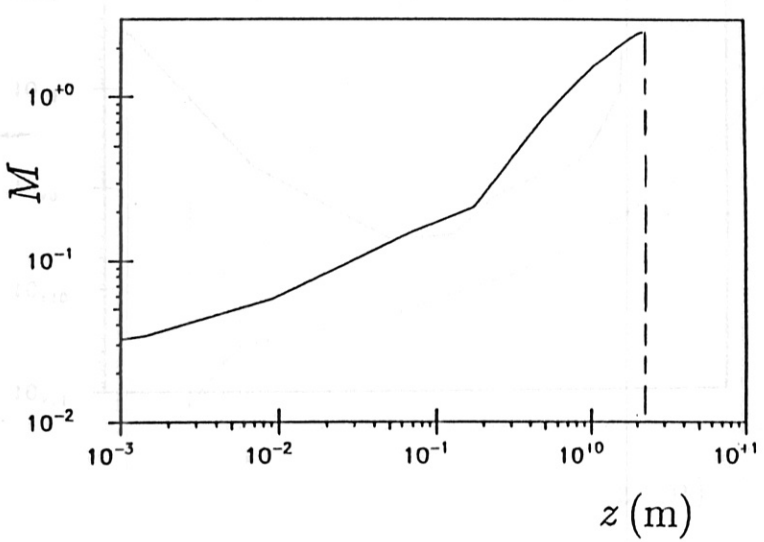

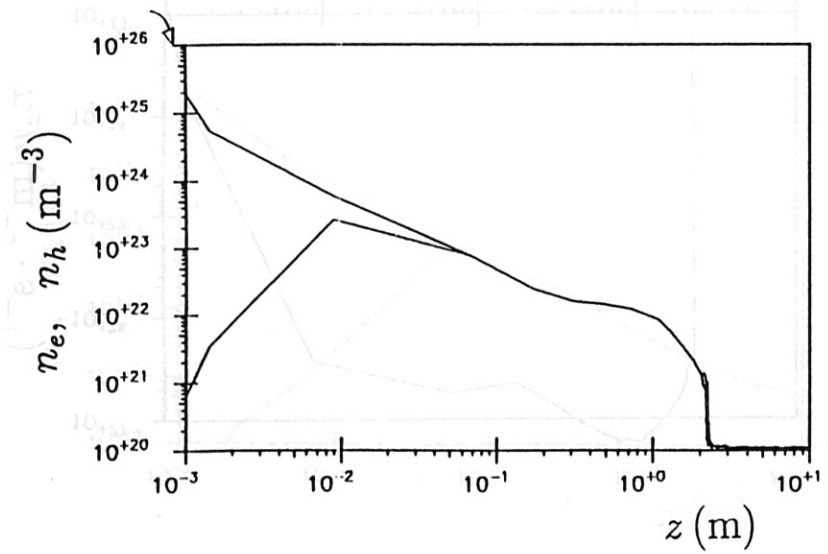

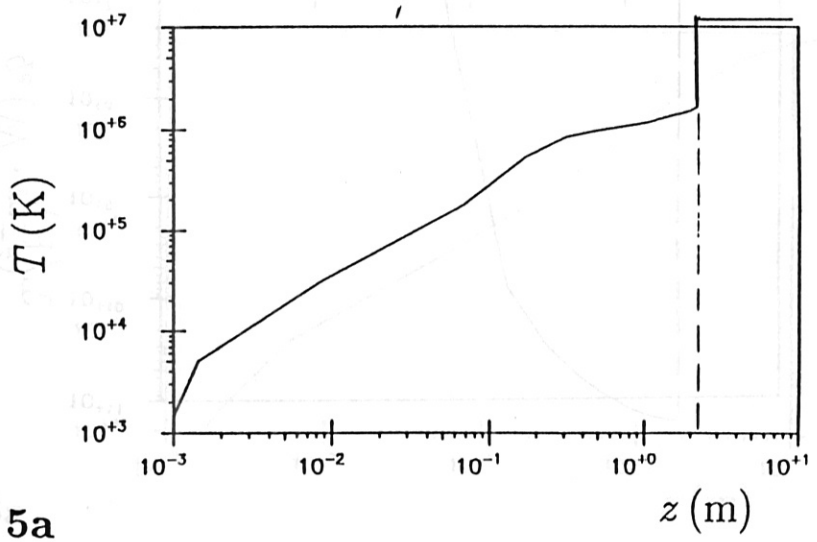

Fig 5a

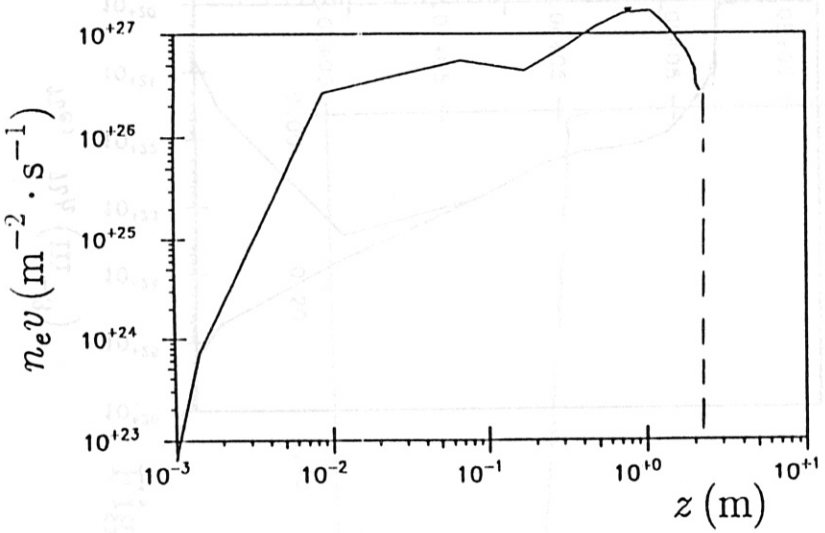
$n_e v\,(\mathrm{m}^{-2}\cdot\mathrm{s}^{-1})$
10^{+27}
10^{+26}
10^{+25}
10^{+24}
10^{+23}
10^{-3}
10^{-2}
10^{-1}
10^{+0}
10^{+1}
$z\,(\mathrm{m})$

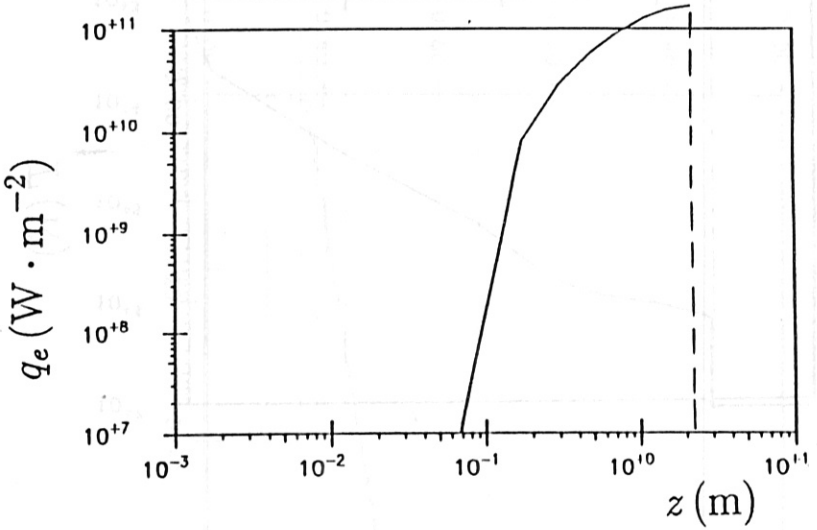
$q_e\,(\mathrm{W}\cdot\mathrm{m}^{-2})$
10^{+11}
10^{+10}
10^{+9}
10^{+8}
10^{+7}
10^{-3}
10^{-2}
10^{-1}
10^{+0}
10^{+1}
$z\,(\mathrm{m})$

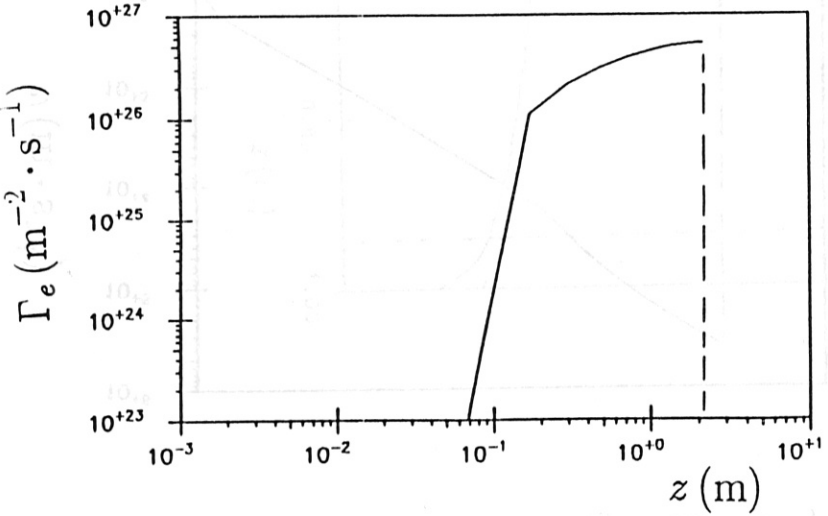
$\Gamma_e\,(\mathrm{m}^{-2}\cdot\mathrm{s}^{-1})$
10^{+27}
10^{+26}
10^{+25}
10^{+24}
10^{+23}
10^{-3}
10^{-2}
10^{-1}
10^{+0}
10^{+1}
$z\,(\mathrm{m})$

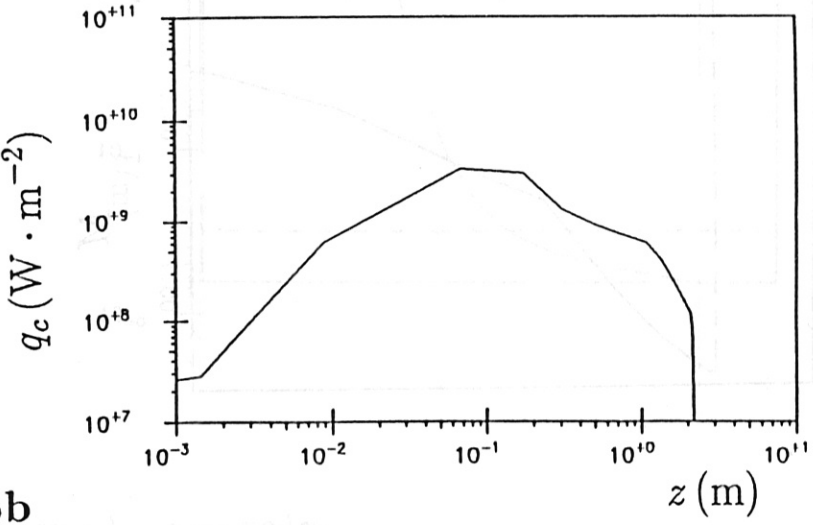
$q_c\,(\mathrm{W}\cdot\mathrm{m}^{-2})$
10^{+11}
10^{+10}
10^{+9}
10^{+8}
10^{+7}
10^{-3}
10^{-2}
10^{-1}
10^{+0}
10^{+1}
$z\,(\mathrm{m})$

Fig 5b

$$\dot{n}_s = 10^{24}\,\mathrm{s}^{-1}, \quad T_e^{\infty} = 1\,\mathrm{keV}, \quad t = 52\,\mu\mathrm{s}$$

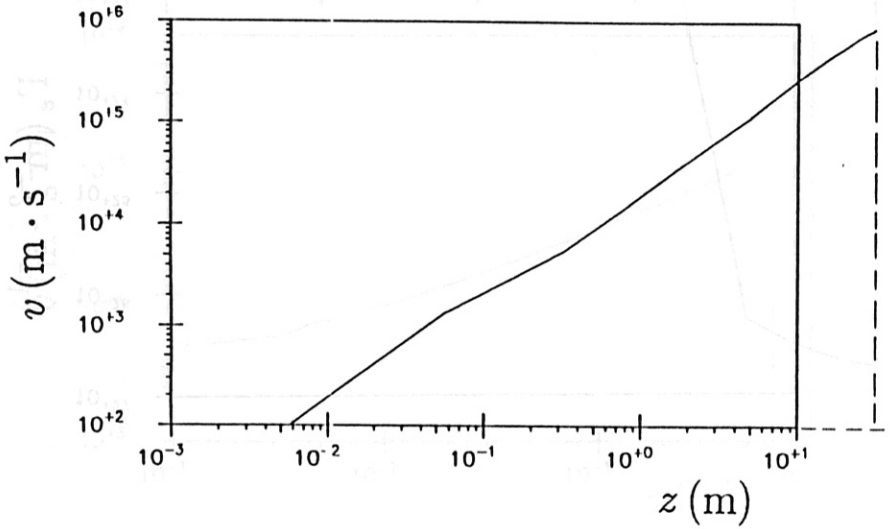

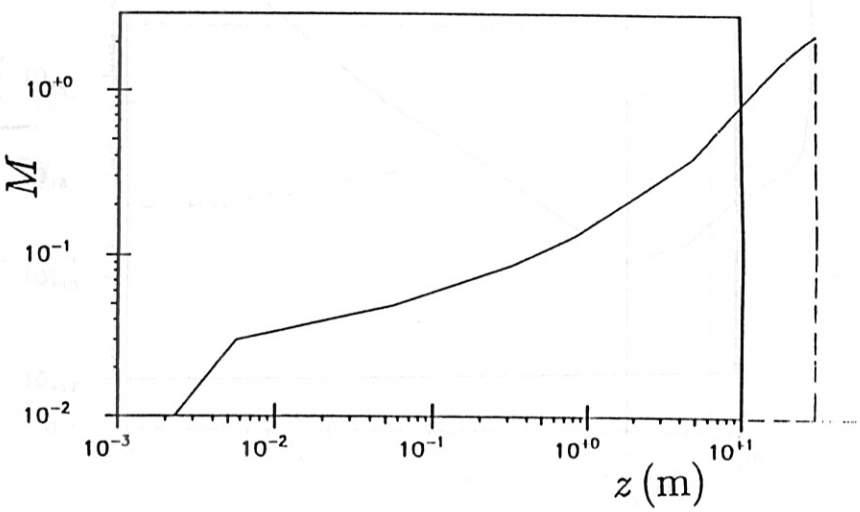

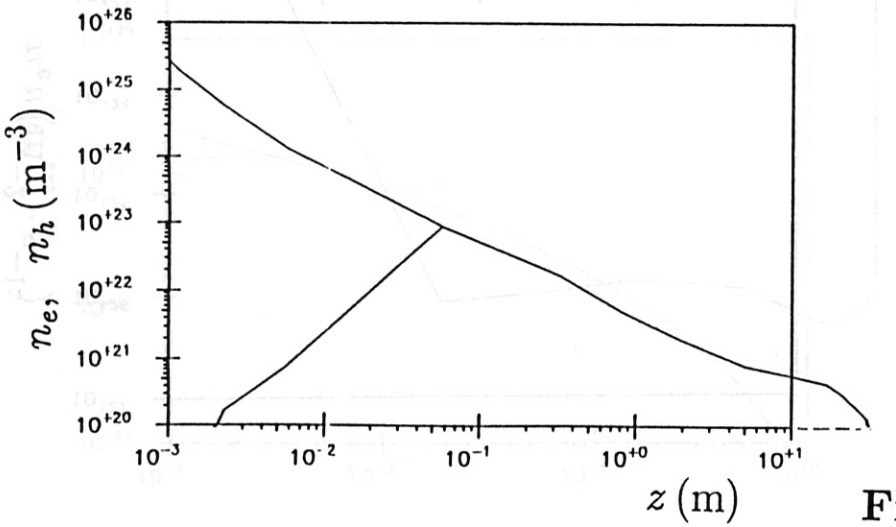

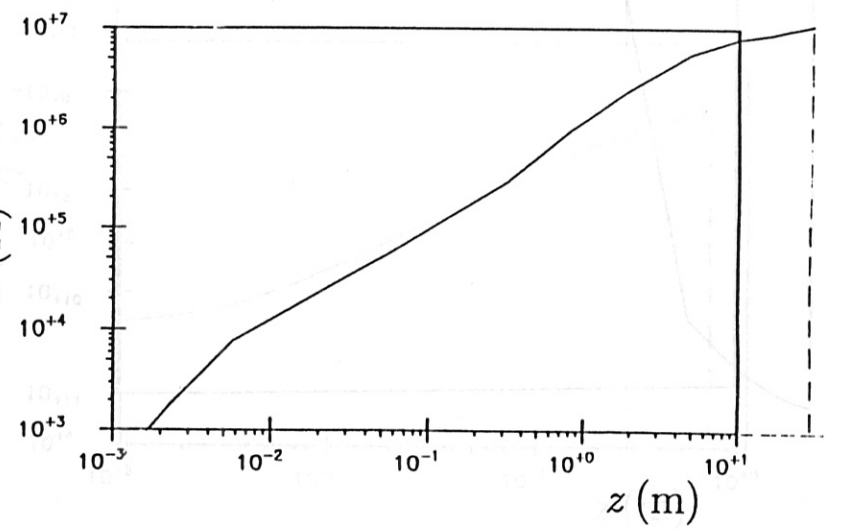

Fig 6a

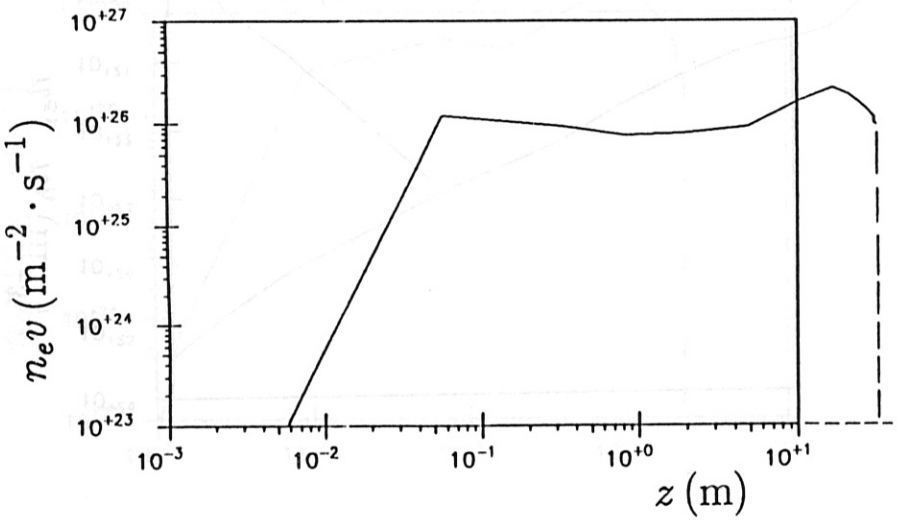
10^{+27}
10^{+26}
10^{+25}
10^{+24}
10^{+23}
$n_e v\,(\mathrm{m}^{-2}\cdot\mathrm{s}^{-1})$
10^{-3}
10^{-2}
10^{-1}
10^{+0}
10^{+1}
$z\,(\mathrm{m})$

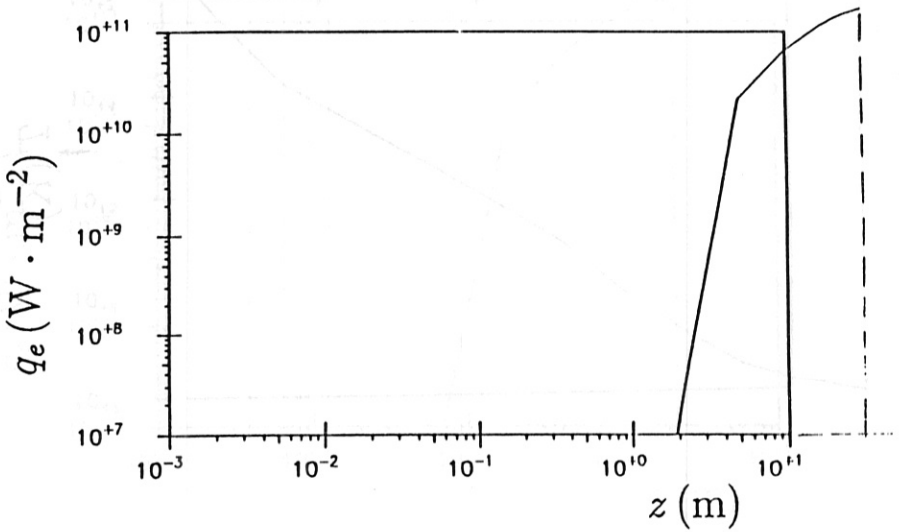
10^{+11}
10^{+10}
10^{+9}
10^{+8}
10^{+7}
$q_e\,(\mathrm{W}\cdot\mathrm{m}^{-2})$
10^{-3}
10^{-2}
10^{-1}
10^{+0}
10^{+1}
$z\,(\mathrm{m})$

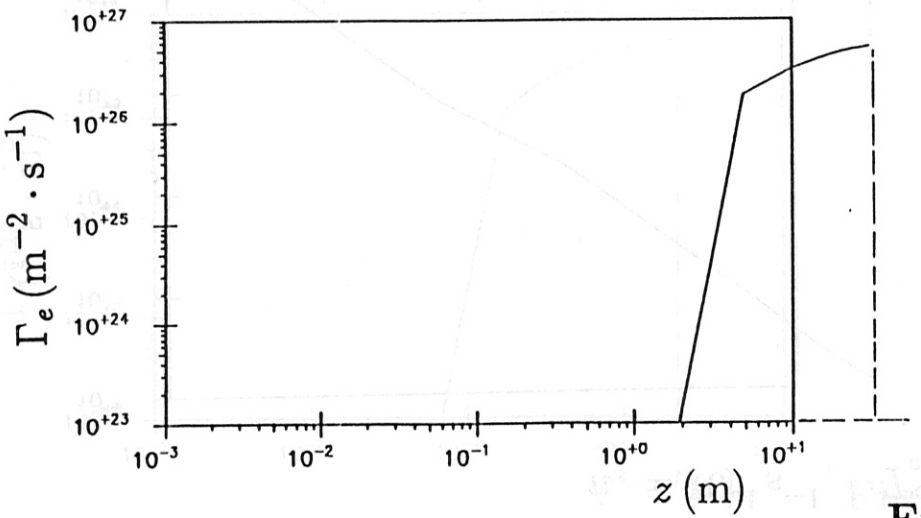
10^{+27}
10^{+26}
10^{+25}
10^{+24}
10^{+23}
$\Gamma_e\,(\mathrm{m}^{-2}\cdot\mathrm{s}^{-1})$
10^{-3}
10^{-2}
10^{-1}
10^{+0}
10^{+1}
$z\,(\mathrm{m})$

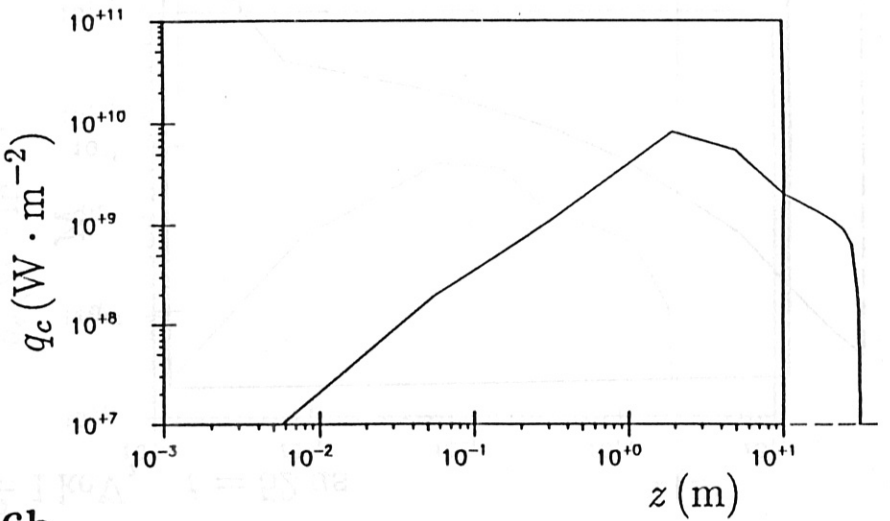
10^{+11}
10^{+10}
10^{+9}
10^{+8}
10^{+7}
$q_c\,(\mathrm{W}\cdot\mathrm{m}^{-2})$
10^{-3}
10^{-2}
10^{-1}
10^{+0}
10^{+1}
$z\,(\mathrm{m})$

Fig 6b

$\dot{n}_s = 10^{24}\,\mathrm{s}^{-1}, \quad T_e^{\infty} = 5\,\mathrm{keV}, \quad t = 7.8\,\mu\mathrm{s}$

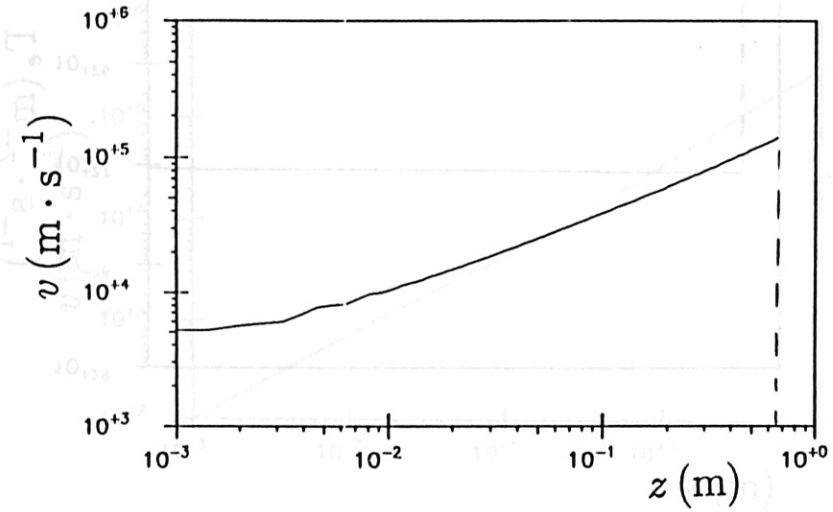

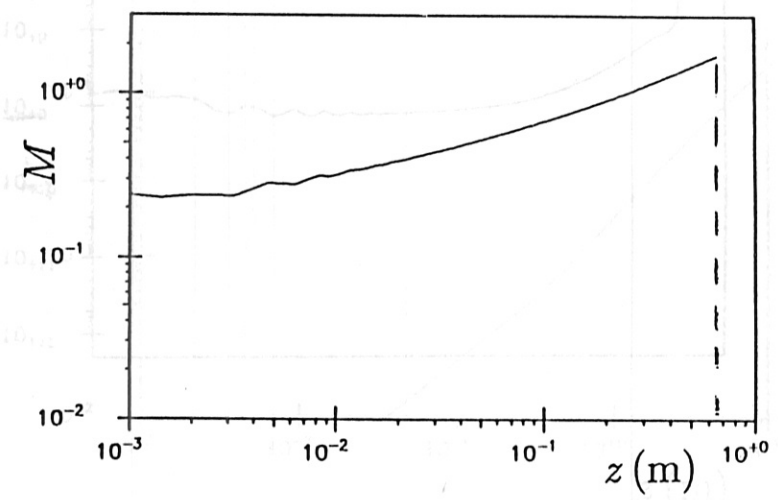

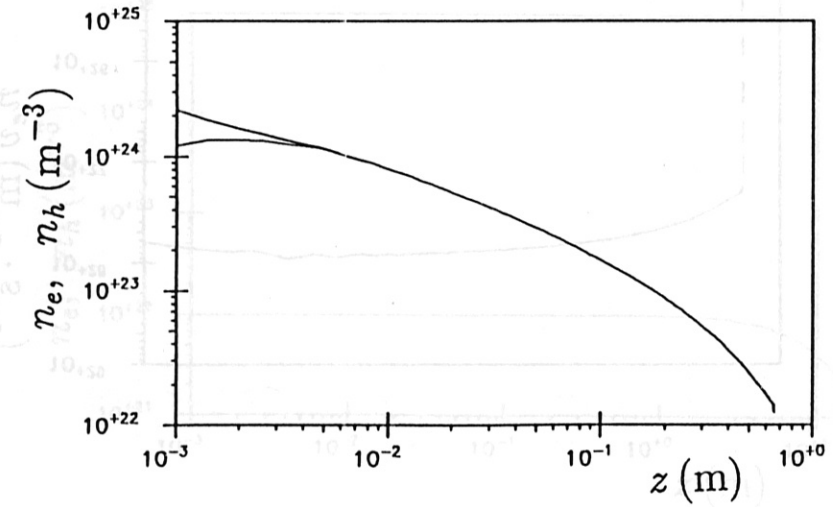

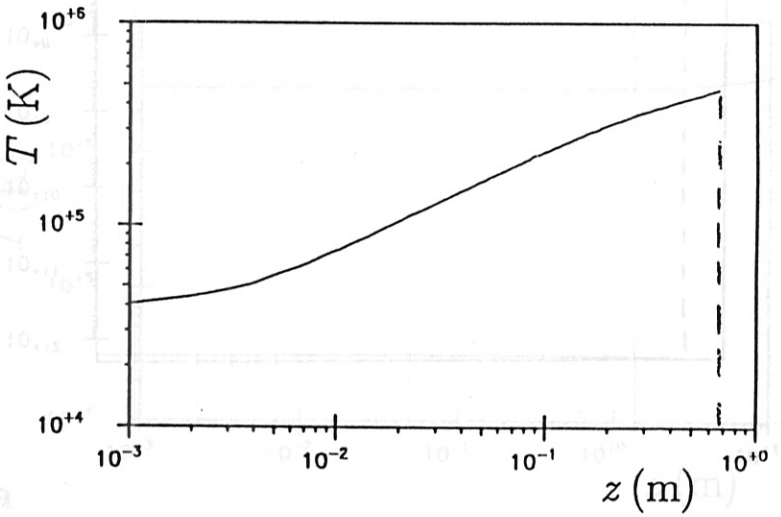

Fig 7a

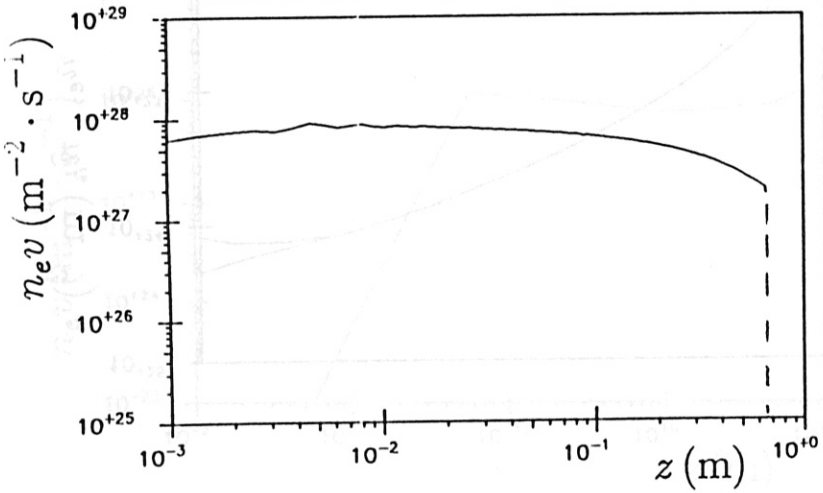
$n_e v\,(\mathrm{m}^{-2}\cdot\mathrm{s}^{-1})$
10^{+29}
10^{+28}
10^{+27}
10^{+26}
10^{+25}
10^{-3}
10^{-2}
10^{-1}
10^{+0}
$z\,(\mathrm{m})$

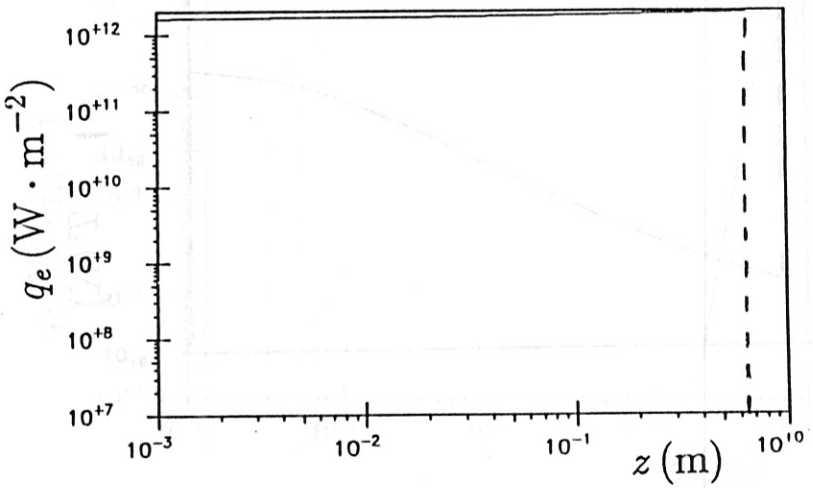
$q_e\,(\mathrm{W}\cdot\mathrm{m}^{-2})$
10^{+12}
10^{+11}
10^{+10}
10^{+9}
10^{+8}
10^{+7}
10^{-3}
10^{-2}
10^{-1}
10^{+0}
$z\,(\mathrm{m})$

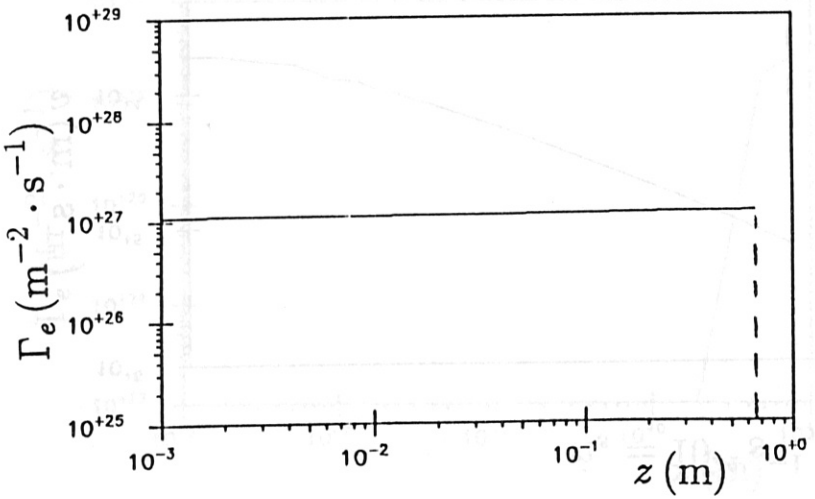
$\Gamma_e\,(\mathrm{m}^{-2}\cdot\mathrm{s}^{-1})$
10^{+29}
10^{+28}
10^{+27}
10^{+26}
10^{+25}
10^{-3}
10^{-2}
10^{-1}
10^{+0}
$z\,(\mathrm{m})$

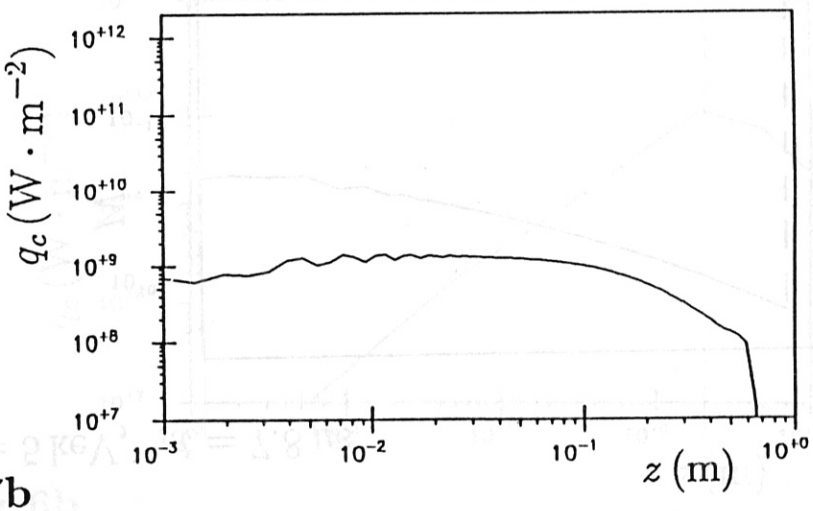
$q_c\,(\mathrm{W}\cdot\mathrm{m}^{-2})$
10^{+12}
10^{+11}
10^{+10}
10^{+9}
10^{+8}
10^{+7}
10^{-3}
10^{-2}
10^{-1}
10^{+0}
$z\,(\mathrm{m})$

Fig 7b

$$\dot{n}_s = 10^{24}\,\mathrm{s}^{-1}, \quad T_e^{\infty} = 5\,\mathrm{keV}, \quad t = 52\,\mu\mathrm{s}$$

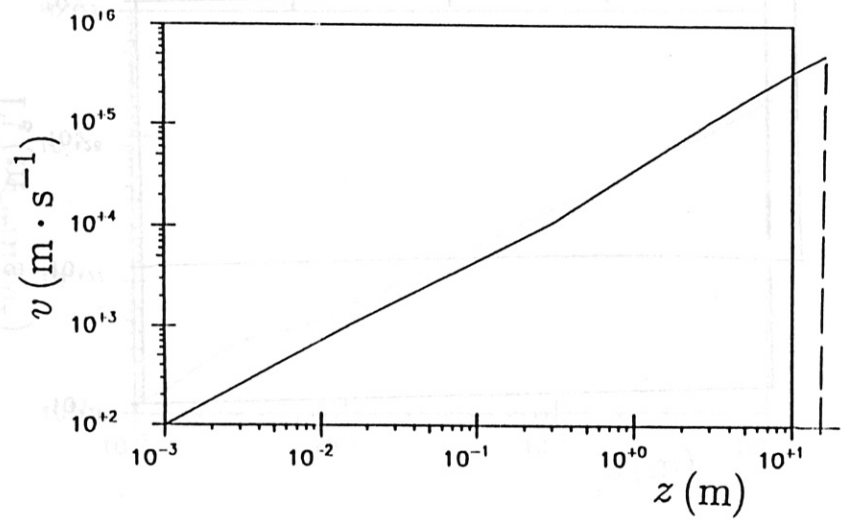

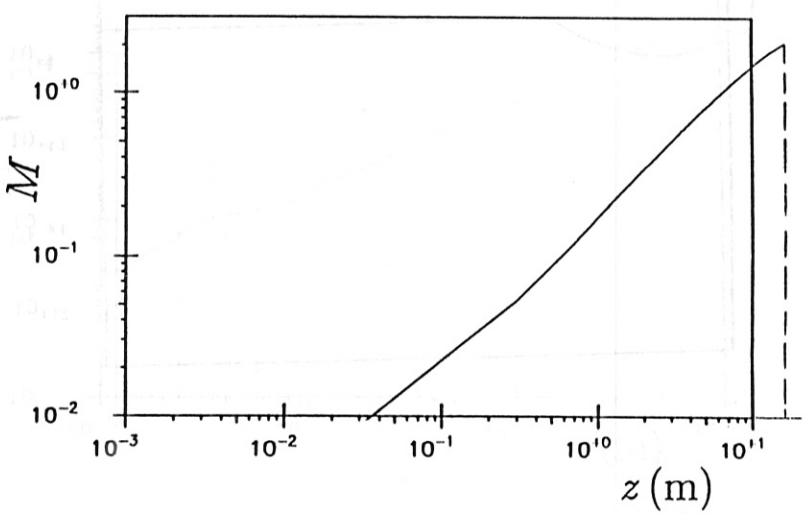

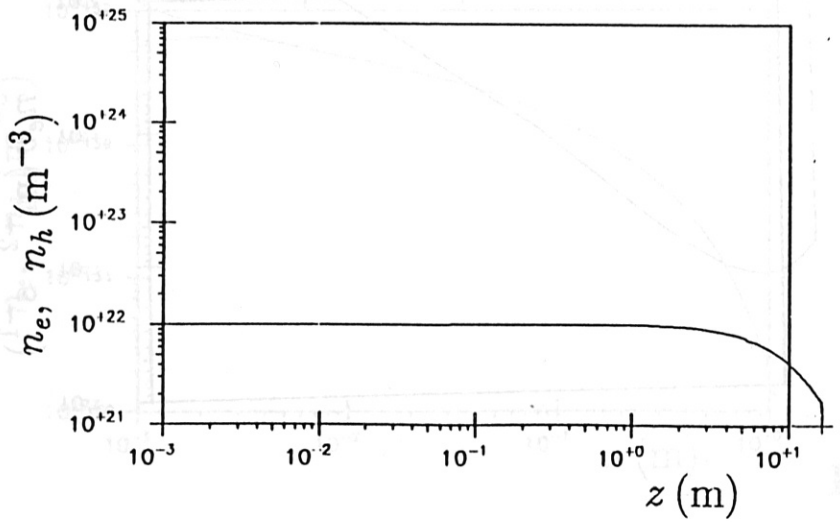

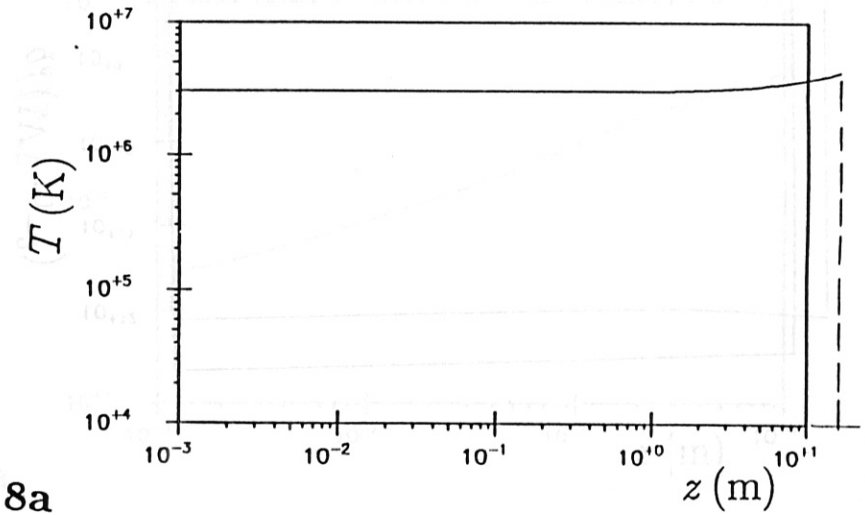

Fig 8a

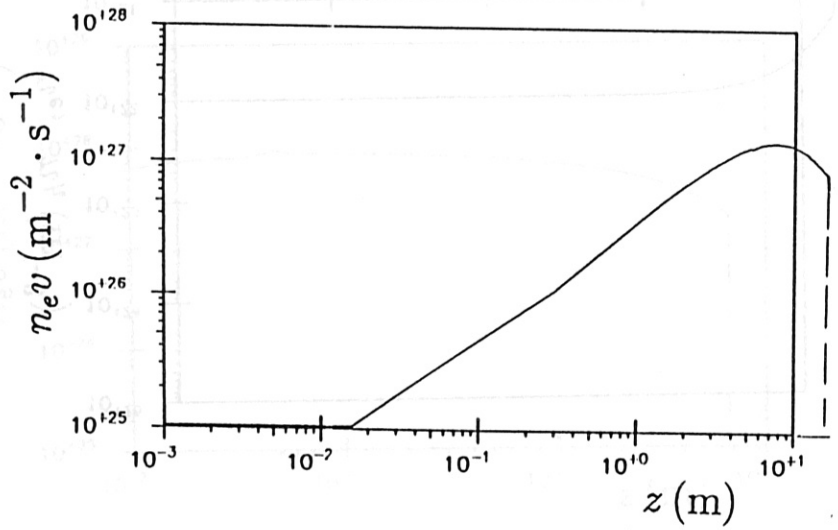
10^{+28}
10^{+27}
10^{+26}
10^{+25}
$n_e v\,(\mathrm{m}^{-2}\cdot\mathrm{s}^{-1})$
10^{-3} 10^{-2} 10^{-1} 10^{+0} 10^{+1}
$z\,(\mathrm{m})$

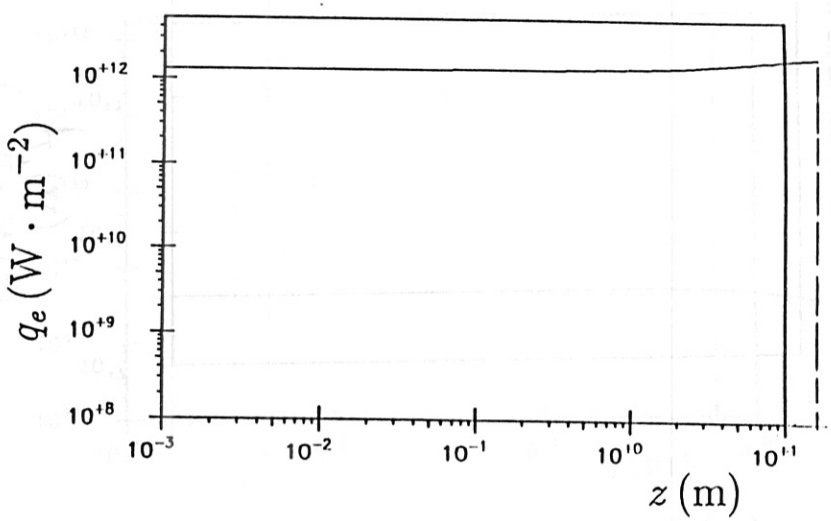
10^{+12}
10^{+11}
10^{+10}
10^{+9}
10^{+8}
$q_e\,(\mathrm{W}\cdot\mathrm{m}^{-2})$
10^{-3} 10^{-2} 10^{-1} 10^{+0} 10^{+1}
$z\,(\mathrm{m})$

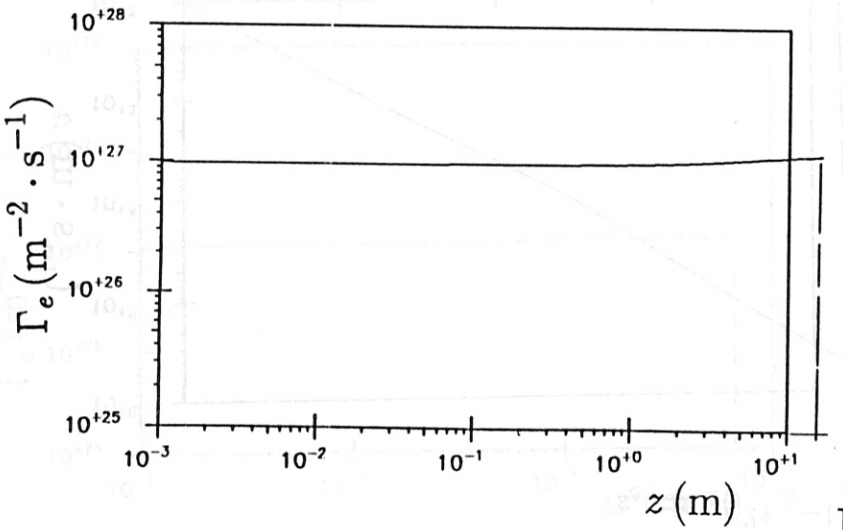
10^{+28}
10^{+27}
10^{+26}
10^{+25}
$\Gamma_e\,(\mathrm{m}^{-2}\cdot\mathrm{s}^{-1})$
10^{-3} 10^{-2} 10^{-1} 10^{+0} 10^{+1}
$z\,(\mathrm{m})$

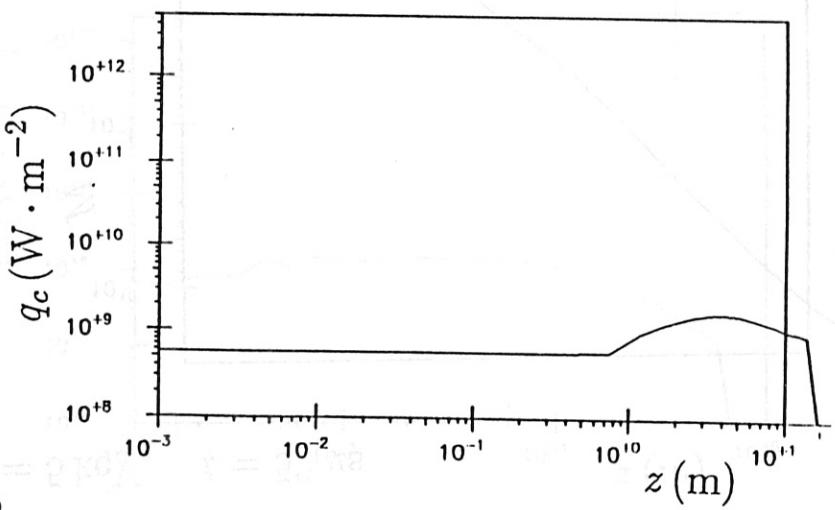
10^{+12}
10^{+11}
10^{+10}
10^{+9}
10^{+8}
$q_c\,(\mathrm{W}\cdot\mathrm{m}^{-2})$
10^{-3} 10^{-2} 10^{-1} 10^{+0} 10^{+1}
$z\,(\mathrm{m})$

Fig 8b

$\dot{n}_s = 10^{25}\,\mathrm{s}^{-1}$, $T_e^{\infty} = 5\,\mathrm{keV}$, $t = 7.7\,\mu\mathrm{s}$

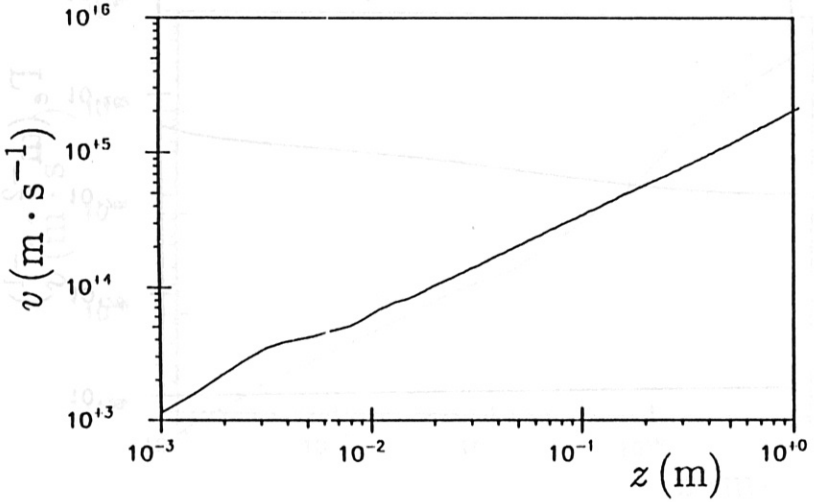

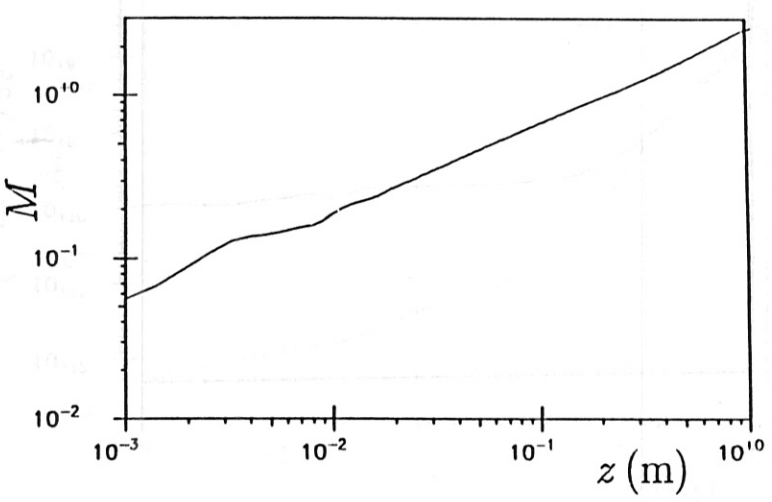

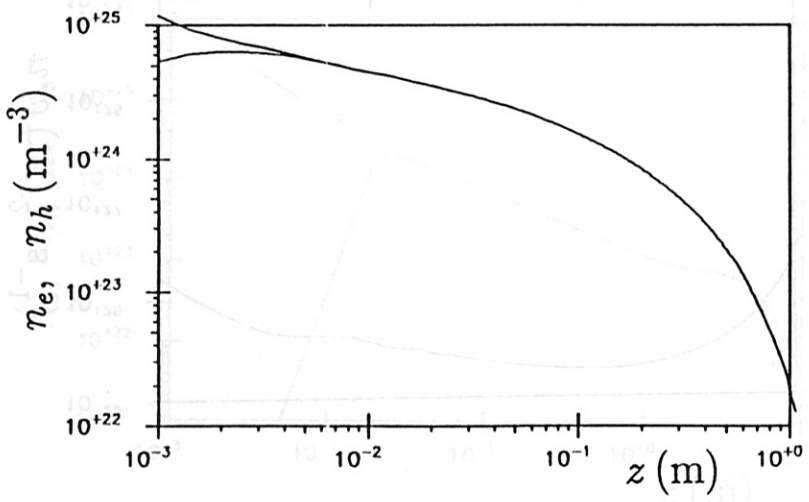

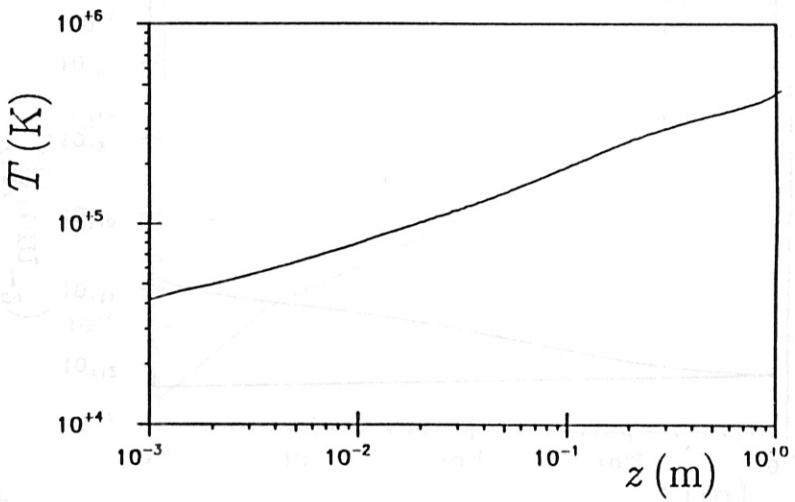

Fig 9a

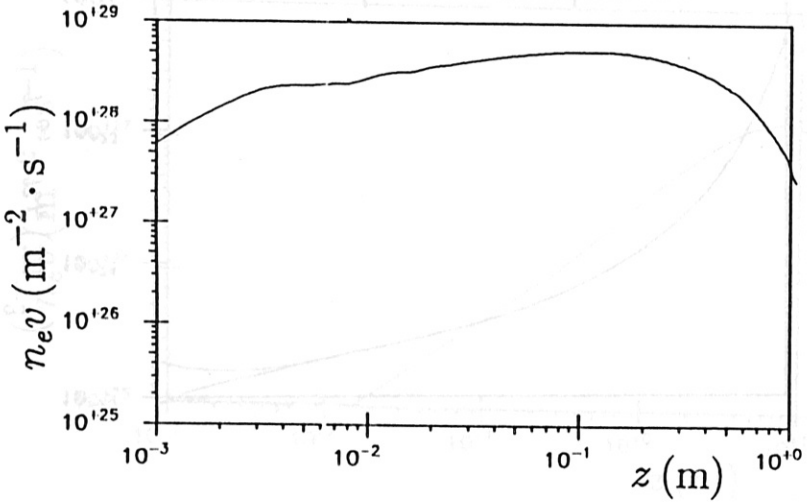
10^{+29}
10^{+28}
10^{+27}
10^{+26}
10^{+25}
$n_e v\,(\mathrm{m}^{-2}\cdot\mathrm{s}^{-1})$
10^{-3}
10^{-2}
10^{-1}
10^{+0}
$z\,(\mathrm{m})$

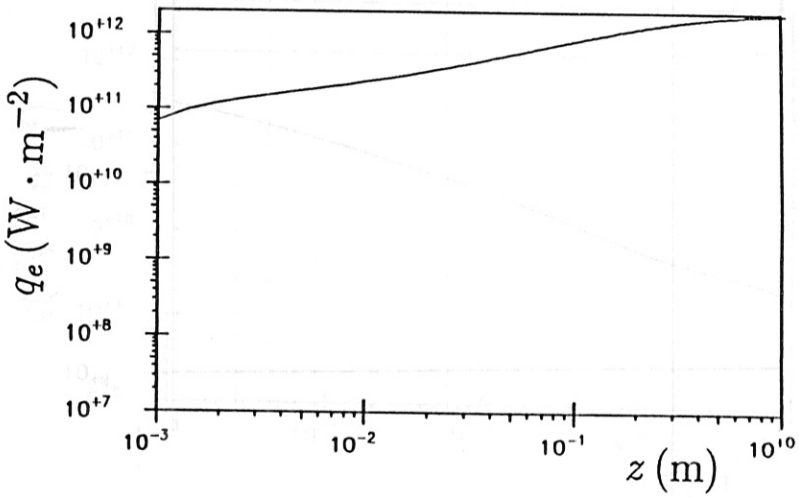
10^{+12}
10^{+11}
10^{+10}
10^{+9}
10^{+8}
10^{+7}
$q_e\,(\mathrm{W}\cdot\mathrm{m}^{-2})$
10^{-3}
10^{-2}
10^{-1}
10^{+0}
$z\,(\mathrm{m})$

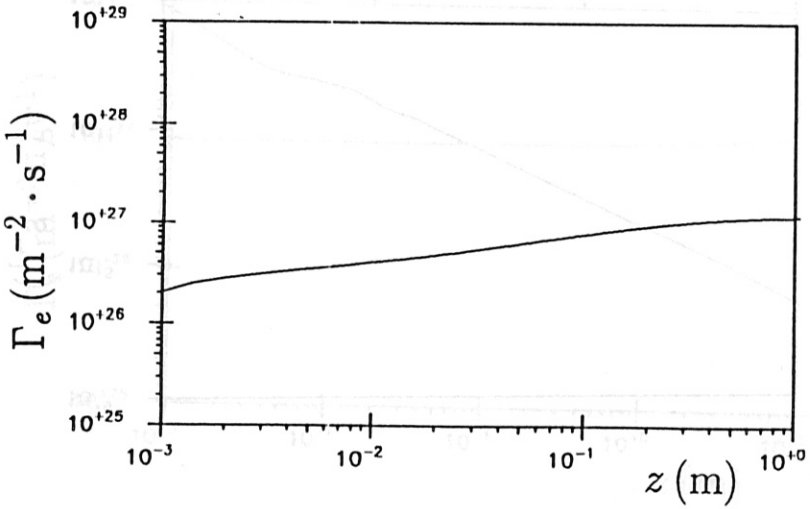
10^{+29}
10^{+28}
10^{+27}
10^{+26}
10^{+25}
$\Gamma_e\,(\mathrm{m}^{-2}\cdot\mathrm{s}^{-1})$
10^{-3}
10^{-2}
10^{-1}
10^{+0}
$z\,(\mathrm{m})$

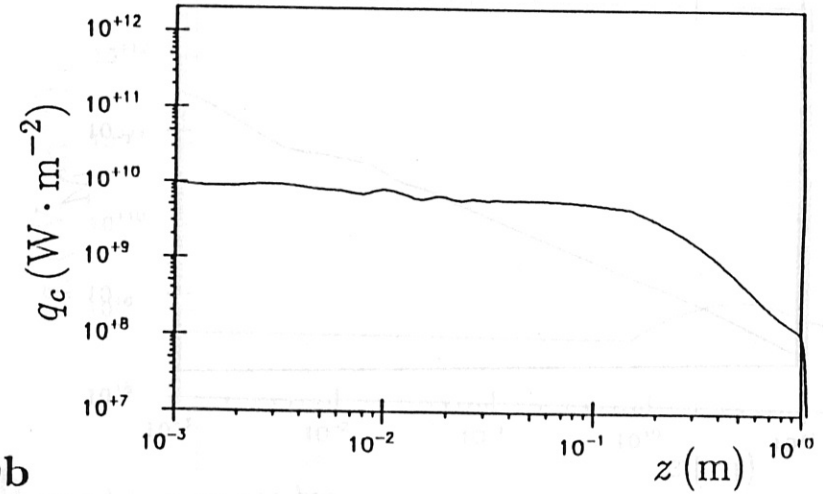
10^{+12}
10^{+11}
10^{+10}
10^{+9}
10^{+8}
10^{+7}
$q_c\,(\mathrm{W}\cdot\mathrm{m}^{-2})$
10^{-3}
10^{-2}
10^{-1}
10^{+0}
$z\,(\mathrm{m})$

Fig 9b

$$\dot{n}_s = 10^{25}\,\mathrm{s}^{-1}, \quad T_e^{\infty} = 5\,\mathrm{keV}, \quad t = 32\,\mu\mathrm{s}$$

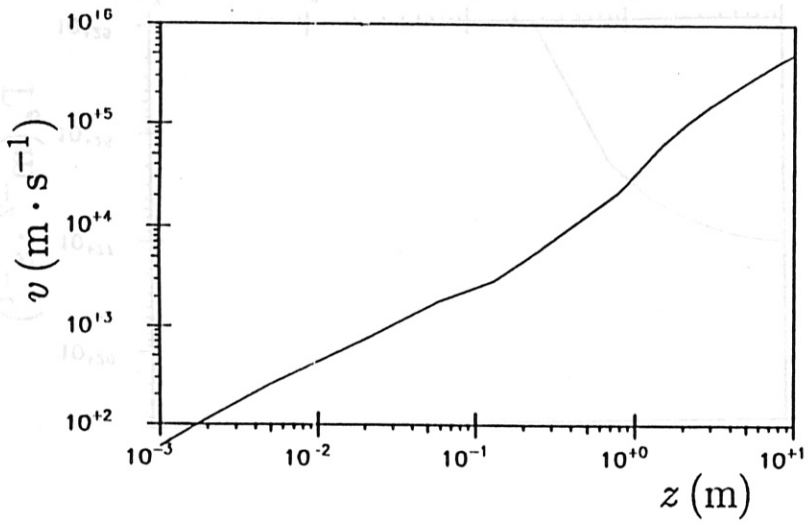

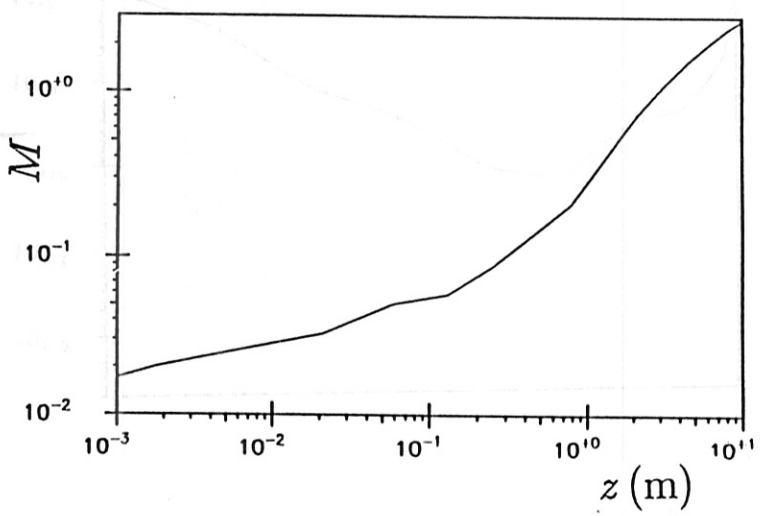

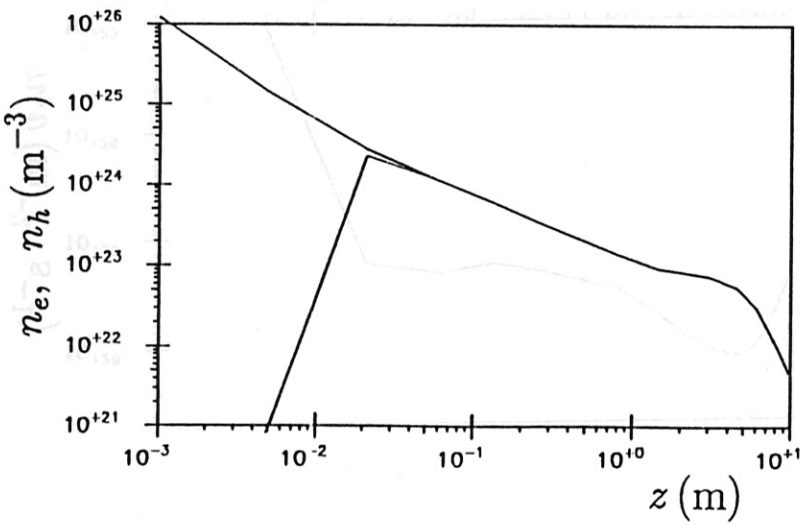

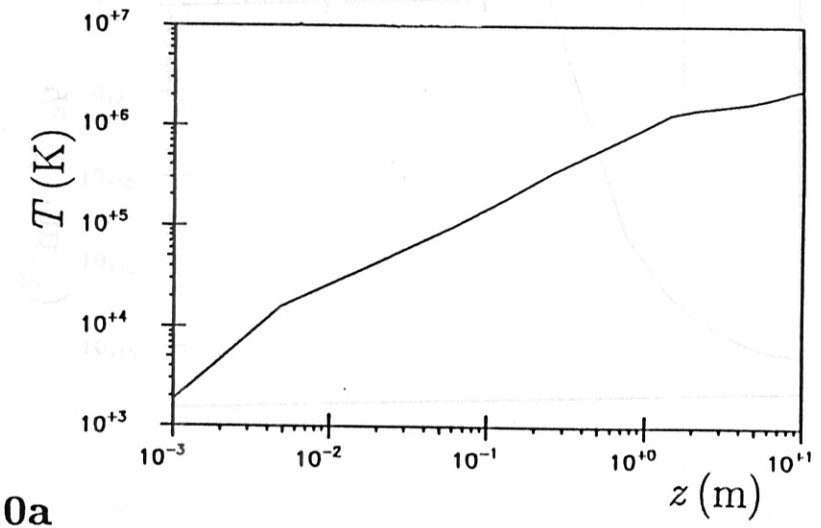

Fig 10a

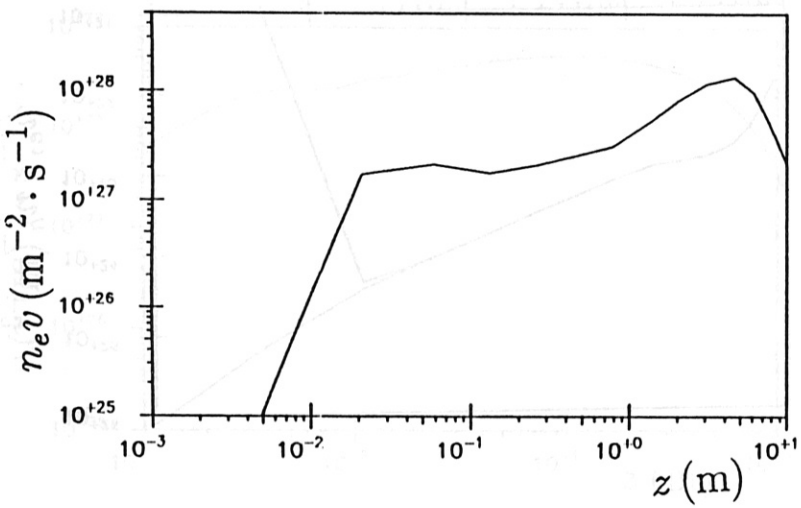
$n_e v\,(\mathrm{m}^{-2}\cdot\mathrm{s}^{-1})$
10^{+28}
10^{+27}
10^{+26}
10^{+25}
10^{-3}
10^{-2}
10^{-1}
10^{+0}
10^{+1}
$z\,(\mathrm{m})$

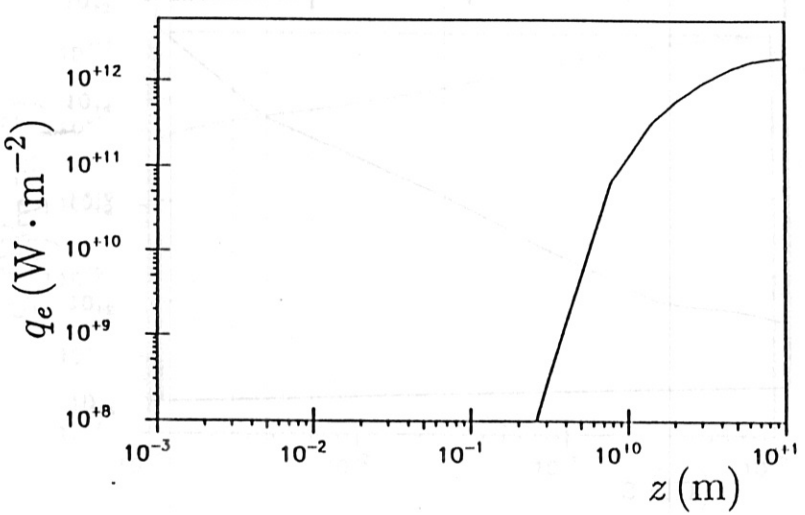
$q_e\,(\mathrm{W}\cdot\mathrm{m}^{-2})$
10^{+12}
10^{+11}
10^{+10}
10^{+9}
10^{+8}
10^{-3}
10^{-2}
10^{-1}
10^{+0}
10^{+1}
$z\,(\mathrm{m})$

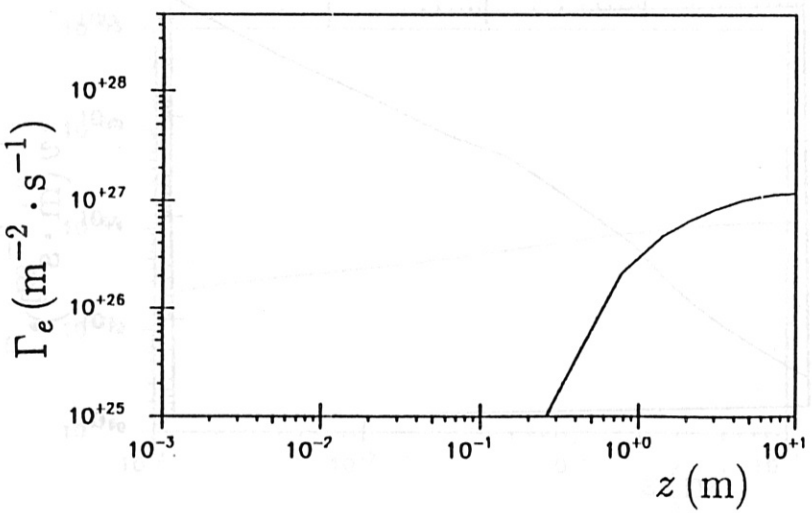
$\Gamma_e\,(\mathrm{m}^{-2}\cdot\mathrm{s}^{-1})$
10^{+28}
10^{+27}
10^{+26}
10^{+25}
10^{-3}
10^{-2}
10^{-1}
10^{+0}
10^{+1}
$z\,(\mathrm{m})$

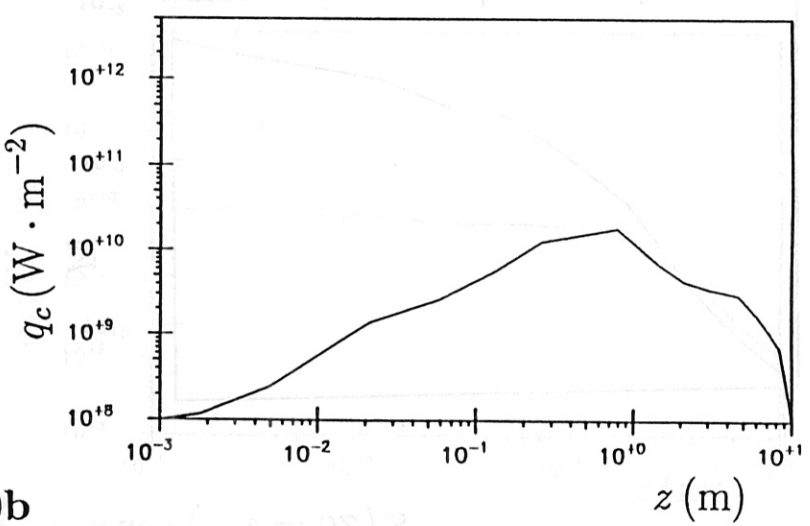
$q_c\,(\mathrm{W}\cdot\mathrm{m}^{-2})$
10^{+12}
10^{+11}
10^{+10}
10^{+9}
10^{+8}
10^{-3}
10^{-2}
10^{-1}
10^{+0}
10^{+1}
$z\,(\mathrm{m})$

Fig 10b